Dual-Polarization Radar Rainfall Estimation over Tropical Oceans

ELIZABETH J. THOMPSON

Applied Physics Laboratory, University of Washington, Seattle, Washington

STEVEN A. RUTLEDGE AND BRENDA DOLAN

Department of Atmospheric Science, Colorado State University, Fort Collins, Colorado

MERHALA THURAI AND V. CHANDRASEKAR

Department of Electrical and Computer Engineering, Colorado State University, Fort Collins, Colorado

(Manuscript received 6 June 2017, in final form 15 December 2017)

ABSTRACT

Dual-polarization radar rainfall estimation relationships have been extensively tested in continental and subtropical coastal rain regimes, with little testing over tropical oceans where the majority of rain on Earth occurs. A 1.5-yr Indo-Pacific warm pool disdrometer dataset was used to quantify the impacts of tropical oceanic drop-size distribution (DSD) variability on dual-polarization radar variables and their resulting utility for rainfall estimation. Variables that were analyzed include differential reflectivity Z_{dr}; specific differential phase K_{dp}; reflectivity Z_h; and specific attenuation A_h. When compared with continental or coastal convection, tropical oceanic Z_{dr} and K_{dp} values were more often of low magnitude ($<$0.5 dB, $<$0.3° km^{-1}) and Z_{dr} was lower for a given K_{dp} or Z_h, consistent with observations of tropical oceanic DSDs being dominated by numerous, small, less-oblate drops. New X-, C-, and S-band R estimators were derived: $R(K_{dp})$, $R(A_h)$, $R(K_{dp}, \zeta_{dr})$, $R(z, \zeta_{dr})$, and $R(A_h, \zeta_{dr})$, which use linear versions of Z_{dr} and Z_h, namely ζ_{dr} and z. Except for $R(K_{dp})$, convective/stratiform partitioning was unnecessary for these estimators. All dual-polarization estimators outperformed updated $R(z)$ estimators derived from the same dataset. The best-performing estimator was $R(K_{dp}, \zeta_{dr})$, followed by $R(A_h, \zeta_{dr})$ and $R(z, \zeta_{dr})$. The R error was further reduced in an updated blended algorithm choosing between $R(z)$, $R(z, \zeta_{dr})$, $R(K_{dp})$, and $R(K_{dp}, \zeta_{dr})$ depending on $Z_{dr} > 0.25$ dB and $K_{dp} > 0.3°$ km^{-1} thresholds. Because of these thresholds and the lack of hail, $R(K_{dp})$ was never used. At all wavelengths, $R(z)$ was still needed 43% of the time during light rain ($R < 5$ mm h^{-1}, $Z_{dr} < 0.25$ dB), composing 7% of the total rain volume. As wavelength decreased, $R(K_{dp}, \zeta_{dr})$ was used more often, $R(z, \zeta_{dr})$ was used less often, and the blended algorithm became increasingly more accurate than $R(z)$.

1. Introduction

Dual-polarization radar rain estimators have been tested almost entirely in continental and subtropical coastal rain regimes (Sachidananda and Zrnić 1986, 1987; Chandrasekar et al. 1990; Aydin and Giridhar 1992; Scarchilli et al. 1993; Carey and Rutledge 2000; Zrnić et al. 2000; Bringi and Chandrasekar 2001, hereinafter BC01; Keenan et al. 2001; Brandes et al. 2002; Ryzhkov et al. 2005b; Park et al. 2005; Matrosov et al. 2006; Gu et al. 2011; Bringi et al. 2011), yet the majority of rain falls over tropical oceans. To accurately quantify the energy and water cycles fueling the global circulation, tropical oceanic rainfall needs to be understood with considerable accuracy (Hartmann et al. 1984; Johnson et al. 1999; Schumacher et al. 2004; Hegerl et al. 2015). Satellites quantify rain over tropical and midlatitude oceans operationally (e.g., Tan et al. 2017; Skofronick-Jackson et al. 2017), but at a coarser spatial and temporal resolution than individual evolving storm components (Yuter and Houze 1998). Compared to satellites, higher-resolution radars can be equipped on ocean-going research vessels (Hudlow 1979; Short et al. 1997; Xu and Rutledge 2014), which can now measure dual-polarization quantities [the new CSU seafaring polarimetric (SEA-POL) 5-cm radar].

Corresponding author: Elizabeth J. Thompson, eliz@apl.uw.edu

DOI: 10.1175/JAMC-D-17-0160.1

Dual-polarization radars can estimate rain rate R more accurately than can single-polarization radars because the former can constrain environmental controls on rain variability with multiple variables: reflectivity Z_h; specific differential phase K_{dp}; attenuation of the horizontally polarized radar signal A_h; and differential reflectivity Z_{dr} instead of one: horizontally polarized radar reflectivity Z_h (Seliga and Bringi 1976; Sachidananda and Zrnić 1987; Carey and Rutledge 2000; Carey et al. 2000; BC01; Schuur et al. 2001; Ryzhkov et al. 2005a,b,c; Kumjian 2013a,b,c). The quantities K_{dp}, A_h, Z_{dr}, Z_h, and R are related to raindrop-size distribution (DSD) parameters, which include the liquid water content LWC; median drop diameter D_0; and proxy for number concentration N_W (BC01; Schuur et al. 2001; Brandes et al. 2002). These DSD parameters vary with each other in systematic ways depending on cloud microphysical processes, which are related to atmospheric instability, aerosol contents, humidity, and temperature (Pruppacher and Klett 1997; BC01; Steiner et al. 2004; Cotton et al. 2011). These cloud processes lead to characteristically different modes of DSD parameter variability in stratiform and convective rain (Tokay and Short 1996; Houze 1997; Cifelli et al. 2000; Bringi et al. 2003, 2009; Thurai et al. 2010; Schumacher et al. 2015; Thompson et al. 2015, hereinafter T15), as well as differences between convective rain DSDs in tropical, subtropical, or midlatitude air masses over the ocean, coasts, or land (Zipser 2003; Bringi et al. 2003, 2006, 2009; Ryzhkov et al. 2005a; Munchak et al. 2012; T15; Houze et al. 2015; Liu and Liu 2016).

Convective rain over tropical oceans is dominated by more numerous, smaller-diameter, and therefore less oblate raindrops compared to stratiform rain or continental convection that contains more vigorous ice-based processes including riming (BC01; Bringi et al. 2003, 2009; Ryzhkov et al. 2005a,b; Thurai et al. 2010; Rowe and Houze 2014; T15). How does the unique DSD variability of tropical oceanic rain affect the dual-polarization radar variables? Smaller, less oblate raindrops should result in lower K_{dp} and Z_{dr} for a given LWC. This hypothesis is motivated by observations of relatively low near-surface Z_{dr}, Z_h, and K_{dp} in the central Indian Ocean ($Z_h < 55$ dBZ, $Z_{dr} < 3$ dB, and $K_{dp} < 3°\,km^{-1}$ at S band; Rowe and Houze 2014; T15) and in a reforming tropical depression over Oklahoma compared to typical continental convection (Ryzhkov et al. 2005b).

It is also important to determine how often Z_{dr} and K_{dp} are below data quality thresholds during tropical oceanic rain, which would foil the opportunity to use these variables for radar R estimation. In the midlatitudes, Z_{dr} is used for rainfall estimation when it is above 0.5 dB (i.e., when $R > 6\,mm\,h^{-1}$), and K_{dp} is used if it is above $0.3°\,km^{-1}$, that is, when $Z_h > 38$ dBZ and $R > 50\,mm\,h^{-1}$ (for S band; Ryzhkov et al. 2005b,c; Matrosov et al. 2006; Cifelli et al. 2011, hereinafter C11). The linearized versions of Z_h and Z_{dr} are z and ζ_{dr}. If Z_{dr} exceeds the noise threshold ($Z_{dr} > 0.5$ dB) and R is greater than about $6\,mm\,h^{-1}$, $R(z, \zeta_{dr})$ has been shown to be a superior R estimator compared to $R(z)$ (Gorgucci et al. 1994; Ryzhkov and Zrnić 1995; Ryzhkov et al. 1997). When K_{dp} exceeds its noise threshold, $R(K_{dp})$ and especially $R(K_{dp}, \zeta_{dr})$ relations yield even lower R error and better goodness of fit compared to $R(z)$ or $R(z, \zeta_{dr})$ (Chandrasekar et al. 1990; Bringi et al. 2001; Ryzhkov and Zrnić 1995; Matrosov et al. 2006).

More recently, $R(A_h)$ relations have been successfully implemented at the X, C, and S bands, such that A_h can be estimated from z in combination with the differential propagation phase Φ_{dp} (Bringi et al. 1990; Testud et al. 2000). Since $R(A_h)$ is less sensitive to DSD variations than $R(z)$ or $R(K_{dp})$, R estimators based on A_h have produced lower R errors than R estimators based on z or K_{dp} alone at the X, C, and S bands in several coastal and continental rain regimes (Ryzhkov et al. 2014; Wang et al. 2014; Giangrande et al. 2014; Boodoo et al. 2015; Diederich et al. 2015a,b). These studies explain why estimation of A_h from Φ_{dp} also implies that the resulting A_h and $R(A_h)$ fields are unaffected by radar calibration, partial beam blockage, or wet radomes (unlike Z_{dr} and Z_h) and that A_h and $R(A_h)$ estimations do not rely on a spatial filter (unlike K_{dp}). While temperature is known to impact A_h, Diederich et al. (2015a) found that temperature does not significantly impact $R(A_h)$.

Optimization algorithms have been designed to automatically determine the optimal R relationship depending on rain intensity, radar measurement uncertainty, and raindrop-size distribution variability (Chandrasekar et al. 1993; Ryzhkov et al. 2005b,c; C11; Thurai et al. 2017). Herein, we develop and test new R estimators using z, ζ_{dr}, K_{dp}, and A_h, and we also test several of these relationships in an updated version of an optimization algorithm, the so-called blended algorithm by C11.[1]

The $R(K_{dp})$, $R(z, \zeta_{dr})$, and $R(K_{dp}, \zeta_{dr})$ relationships and their use in optimization algorithms have not been comprehensively tested over open tropical oceans at all three weather radar wavelengths: X, C, and S bands. C-band $R(K_{dp})$ and $R(A_h)$ relations were formed for typhoon rainfall (Wang et al. 2013, 2014) and an S-band

[1] The name of the blended algorithm (C11) does not imply that radar data are actually blended as in Pepler et al. (2011) and Pepler and May (2012).

relation for $R(z, \zeta_{dr})$ was tested over Kwajalein Atoll (Bringi et al. 2012). Since K_{dp} is inversely proportional to radar wavelength, its utility for rainfall estimation could increase at X- and C-band wavelengths relative to S band (Matrosov et al. 2006). However, this potential benefit has not been quantified over tropical oceans in comparison to potentially degrading non-Rayleigh scattering effects (BC01). It also remains unclear whether any of the dual-polarization R relationships require convective/stratiform (C/S) partitioning. Evidence shows that separate $R(z)$ equations fit to stratiform and convective rain over tropical oceans improve radar rainfall estimation there (T15). Dual-polarization R relationships with Z_{dr}, K_{dp}, and A_h are thought to implicitly account for C/S DSD variability better than Z_h alone (BC01; Ryzhkov et al. 2005b). However, an error analysis between dual-polarization R relationships fit to all rain or to C/S rain has not been carried out over tropical oceans.

To quantify the impacts of tropical oceanic DSD variability on K_{dp}, Z_{dr}, A_h, and Z_h, as well as their resulting utility for radar rainfall estimation, a long-term west Pacific Ocean DSD dataset is used to simulate these dual-polarization radar variables (section 2). Radar variables are analyzed within the context of C/S DSD variability (section 3). New R equations are developed, compared, and tested in an updated blended optimization algorithm at X-, C-, and S-band radar wavelengths. The goodness of fit, root-mean-square error, and percent difference of total rain of dual- and single-polarization radar estimators are compared at each λ to determine how, how much, and above which R values dual-polarization radars may improve R estimation over tropical oceans compared to the $R(z)$ methods (section 4).

2. Data and methodology

This study uses 18 months of equatorial west Pacific (Manus Island, 2°S, 147°E) two-dimensional video disdrometer (2DVD) data from the DOE Atmospheric Radiation Measurement Program (http://www.archive.arm.gov/discovery/). The 2DVD is described by Schönhuber et al. (2007, 2008). The 2DVD dataset used in this study was explained and used by T15, who found similar DSD spectra and DSD variability from 2DVD at this west Pacific site and at another central equatorial Indian Ocean site at Gan Island. Rain events at both isolated, open-ocean sites are dominated by the intertropical convergence zone and the Madden–Julian oscillation. As shown by T15, results herein from the Manus Island dataset are representative of the collective Indo-Pacific warm pool.

The data-processing and C/S rain-partitioning techniques in this study are the same as in T15. Following data quality considerations suggested by Tokay et al. (2001, 2005, 2013), Larsen and O'Dell (2016), and Smith (2016), the analyzed dataset had a sufficiently large sample size ($n = 27\,179$) of 1-min DSDs, each containing at least 100 total drops and $R > 0.05\,\text{mm}\,\text{h}^{-1}$. Data extend from 2 December 2011 to 21 April 2013, which spans 1.5 yr. The normalized gamma DSD parameters were computed from this dataset by T15 (see details within). DSD parameters include the intercept parameter or proxy for the number concentration (N_W, drops per meter cubed volume per millimeter size bin), median diameter (D_0, mm), and maximum diameter (D_{MAX}, mm). The liquid water content (LWC, $\text{g}\,\text{m}^{-3}$) and rain rate (R, $\text{mm}\,\text{h}^{-1}$) were calculated directly from the 2DVD by measuring the fall speed of each drop per unit catchment area. Data were separated into convective and stratiform samples based on the optimized $\log_{10}N_W^{SEP} = 3.85$ separation line method from T15, which was verified with 372 case studies of collocated 2DVD DSD and dual-polarization radar data. DSDs were shown to be convective (stratiform) if $\log_{10}N_W$ was greater (less) than $\log_{10}N_W^{SEP}$.

T15 conducted electromagnetic scattering simulations from these DSDs to estimate the radar reflectivity at horizontal polarization (Z_h), specific attenuation (A_h), specific differential phase (K_{dp}), and differential reflectivity (Z_{dr}) at X, C, and S bands (i.e., 3.3, 5.5, and 10.0 cm λ) (see BC01 for review of dual-polarization variables). These scattering simulations led to the creation and testing of new $R(z)$ estimators for all, convective, and stratiform rain over tropical oceans in T15. The quantity Z_h is dependent on the drop diameter D^6 and the number density $N(D)$. For spherical hydrometeors Z_{dr} is zero and becomes more positive as raindrops become more oblate, which usually occurs as $D > 1$ mm. The quantity K_{dp} is directly proportional to the liquid or ice water content of the nonspherical hydrometeors and mean particle oblateness within the radar volume, and inversely proportional to the wavelength λ such that K_{dp} is about 3 times as great at X band as at S band. In the Rayleigh-scattering regime, A_h increases with decreasing temperature and increasing liquid water content (Jameson 1992; BC01). To account for the complex index of refraction, scattering simulations of these variables were performed at 20°C, a typical mean tropical warm pool temperature and the same value used by BC01 and Giangrande et al. (2014). Simulations were for liquid drops viewed at a 1° elevation angle. Simulations account for changing raindrop shape as a function of diameter according to the Thurai et al. (2007) model, assuming raindrops fell at a 0° mean canting angle with a standard deviation up to 7.5° (Huang et al. 2008). No

sampling errors associated with actual radar measurements are included in any of the statistics or error analysis conducted in this study. Electromagnetic scattering simulation assumptions constrain all simulated radar variable ranges such that more variability or spread is expected in real radar-based measurements compared to simulated values, particularly in K_{dp} depending on Φ_{dp} filtering techniques.

Orthogonal linear regression was used to fit new power-law relationships between R and either K_{dp} or A_h; this was also performed by T15 to form updated $R(z)$ equations. Orthogonal linear regression minimizes spread in both the independent and dependent variable parameter spaces, perpendicular to the best-fit line, and yields equivalent $y(x)$ and $x(y)$ equations. Multiple linear least squares regression was used for multiparameter power-law equations: $R(K_{dp}, \zeta_{dr})$, $R(z, \zeta_{dr})$, and $R(A_h, \zeta_{dr})$. Linear versions of reflectivity z and differential reflectivity ζ_{dr} were used in these R equations because of their larger dynamic range. The linear variables were obtained by taking $10^{(0.1 Z_{dr})}$, and the same function for Z_h.

This study makes use of the rain version of the blended optimization algorithm that was first presented by C11. In the rain portion of the C11 algorithm, R was determined throughout the near-surface radar volume by a different R estimator at each radar gate depending on the magnitudes of Z_{dr}, K_{dp}, and Z_h. In its original implementation, which was at S band, the final R value at each radar gate or grid point was determined by the following estimators based on the following rules:

1) $R(z)$ if $Z_{dr} < 0.5$ dB and $K_{dp} < 0.3^\circ$ km^{-1},
2) $R(z, \zeta_{dr})$ if $Z_{dr} > 0.5$ dB and $K_{dp} < 0.3^\circ$ km^{-1},
3) $R(K_{dp})$ if $Z_{dr} < 0.5$ dB and $Z_h > 38$ dBZ and $K_{dp} > 0.3^\circ$ km^{-1}, and
4) $R(K_{dp}, \zeta_{dr})$ if $Z_{dr} > 0.5$ dB and $K_{dp} > 0.3^\circ$ km^{-1}.

These K_{dp} and Z_{dr} thresholds were optimized for implementation of the blended algorithm at S band during continental convection observed in Colorado. The thresholds were designed for data quality reasons in order to prevent application of dual-polarization estimators when dual-polarization measurements do not exceed the expected errors: 0.5 dB for Z_{dr} and 0.3° km^{-1} for K_{dp}. Therefore, the thresholds were designed to be wavelength independent.

The current study updates the C11 blended algorithm thresholds and all four R estimators for application to tropical oceanic rain. T15 produced and tested new $R(z)$ equations using the same DSD dataset employed in the current study. These updated tropical oceanic $R(z)$ equations from T15 are used throughout the current study.

3. Results

a. Simulated dual-polarization variables

This section investigates the impacts of measured tropical oceanic DSD variability on dual-polarization variables: (i) how often Z_{dr} and K_{dp} could be used for rainfall estimation in the CSU blended algorithm (C11) and (ii) how Z_h, K_{dp}, and Z_{dr} relate to each other in response to tropical oceanic DSD variability.

1) Utility for rainfall estimation

Since the tropical oceanic DSDs analyzed in this study were dominated by small drops consistent with prevalent warm rain cloud microphysical processes (T15), 95% of simulated Z_{dr} values were less than 1 dB (95th percentile value); 90% of K_{dp} values remained below 0.7, 0.4, and 0.2° km^{-1} at X, C, and S bands; and Z_h did not exceed 58 dBZ (Fig. 1). These simulated ranges are in agreement with C- and S-band radar observations from TOGA COARE in the equatorial west Pacific and DYNAMO in the central Indian Ocean (Short et al. 1997; Rowe and Houze 2014; Xu and Rutledge 2014; T15). In contrast, continental and coastal convection with melted hail resulting from strong mixed-phase processes can exhibit near-surface $Z_{dr} > 3$ dB, $K_{dp} >$ 1–3 at S band with even higher values at C and X band, and Z_h up to 70 dBZ (BC01; Gatlin et al. 2015).

The simulated tropical oceanic Z_{dr} and K_{dp} values are of interest, especially in comparison to the thresholds of $Z_{dr} = 0.5$ dB and $K_{dp} = 0.3^\circ$ km^{-1} commonly used in midlatitude precipitation estimation algorithms (Fig. 1; Matrosov et al. 2006; C11). DSDs in our sample that were associated with K_{dp} and Z_{dr} below these thresholds contained ample LWC up to 1–2 g m^{-3} (Figs. 2 and 3). At all λs, Z_{dr} exceeded 0.25, 0.5, and 1 dB in only 57%, 32%, and 6% of the dataset. These Z_{dr} values were reached only when at least 5% of the population exceeded $D_{MAX} >$ 1.9, 2.4, or 3.2 mm; $D_0 >$ 1.0, 1.2, or 1.4 mm; and $R >$ 0.5, 0.7, 1.6 mm h^{-1}. The rarity of these conditions motivates lowering the Z_{dr} threshold for tropical oceanic R estimation below 0.5 dB. For the remainder of this study, we consider a Z_{dr} threshold of 0.25 dB, which would increase the utility of Z_{dr} for R estimation while also remaining above the quoted 0.1-dB accuracy, or accepted noise level, of this measurement (Ryzhkov et al. 2005a).

The specific differential phase K_{dp} exceeded 0.3° km^{-1} in only 17%, 11%, or 7% of X-, C-, and S-band data. This occurred when at least 5% of the data exhibited $D_{MAX} >$ 2.4, 2.5, or 2.8 mm; $D_0 >$ 1.2, 1.2, or 1.3 mm; and $R >$ 6, 11, or 21 mm h^{-1} at X, C, and S band, respectively. As

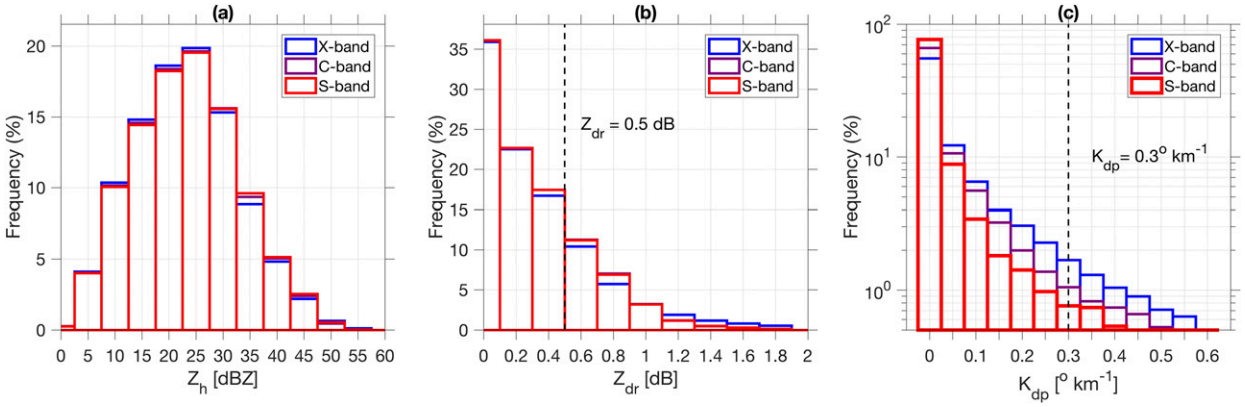

FIG. 1. Simulated (a) Z_h, (b) Z_{dr}, and (c) K_{dp} ranges at X, C, and S band from the equatorial Indo-Pacific warm pool DSD of T15.

restrictive as this 0.3° km^{-1} K_{dp} threshold appears to be over tropical oceans, lowering the K_{dp} data quality threshold below 0.3° km^{-1} is not practical for most radars because of phase instability (BC01). Using the same K_{dp} threshold and a 38-dBZ threshold over Colorado, the C11 blended algorithm was able to use K_{dp} in either the $R(K_{dp})$ or $R(K_{dp}, \zeta_{dr})$ simulations about 20% of the time at S band, 2.8 times more often than expected from this tropical oceanic dataset (at S band). The 0.3° km^{-1} K_{dp} level corresponds to a reflectivity of 34 dBZ at X band, 38 dBZ at C band, and 43 dBZ at S band in this tropical rain regime (K_{dp} = 8.50 × $10^{-5}z^{0.93}$ at C band). Therefore, a 38-dBZ threshold accompanying the 0.3° km^{-1} K_{dp} threshold also appears to be duplicative and unnecessary over tropical oceans.

The frequency of occurrence of meeting both the $K_{dp} > 0.3°\,km^{-1}$ and $Z_{dr} > 0.25$ dB thresholds was the same as that of meeting the K_{dp} threshold alone at each λ because data with K_{dp} of this magnitude already had Z_{dr} of this magnitude or higher. The $Z_{dr} > 0.25$ dB threshold can apparently be met by smaller raindrops and lower LWC than the $K_{dp} > 0.3°\,km^{-1}$ threshold. For instance, if the K_{dp} threshold was unrealistically lowered to 0.1, 0.07, or 0.04 at X, C, and S band, still less than 1% of data would meet a K_{dp} threshold but not a $Z_{dr} > 0.25$ dB threshold. Therefore, there is no theoretical motivation to lower the K_{dp} threshold further below 0.3° km^{-1} in hopes of using $R(K_{dp})$ more often. At any value of K_{dp} that is statistically different from zero, Z_{dr} would also be large enough such that $R(K_{dp}, \zeta_{dr})$, a more accurate estimator (BC01), could be used instead of $R(K_{dp})$.

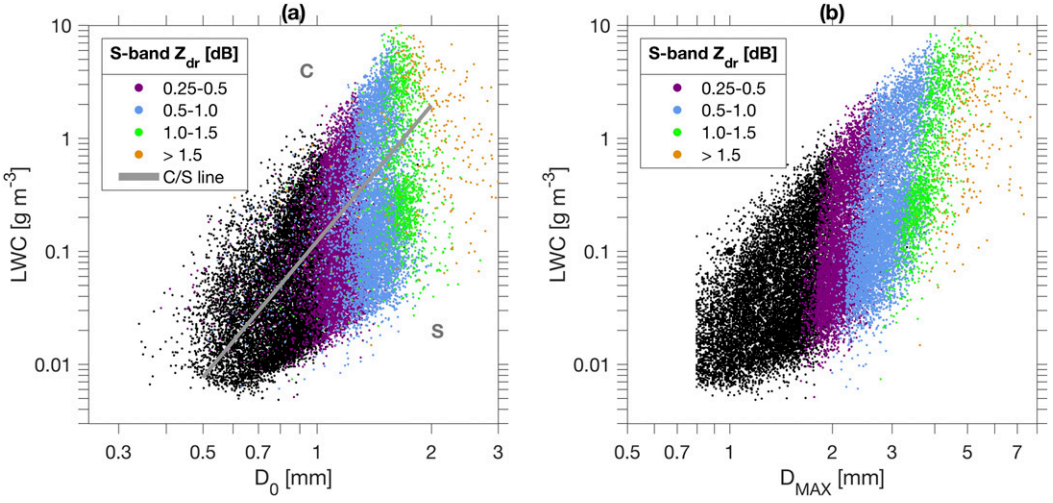

FIG. 2. Indo-Pacific warm pool DSD LWC as a function of (a) median drop diameter D_0 and (b) maximum diameter D_{MAX}, colored by DSD-simulated Z_{dr} at S band. The T15 C/S separation line is plotted in (a) for reference.

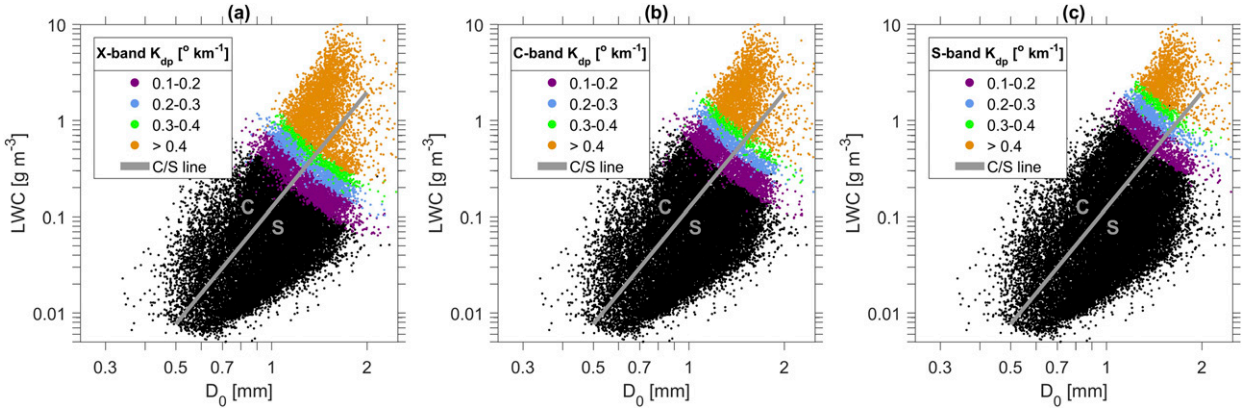

FIG. 3. Indo-Pacific warm pool DSD LWC as a function of median drop diameter D_0, colored by DSD-simulated K_{dp} at (a) X, (b) C, and (c) S bands. The T15 C/S separation line is plotted for reference.

The T15 LWC(D_0) separation line between C/S samples indicates that tropical oceanic convective rain exhibited the same ranges of Z_{dr} as stratiform rain (Fig. 2a) but that convection caused higher K_{dp} for a given D_0 (Fig. 3). This is consistent with findings by T15 that maritime convective and stratiform drop diameter ranges overlap substantially but that convective DSDs contain more LWC and higher N_W for a given D_0. Because of their greater LWC, 77%, 86%, and 90% of the DSD in which X-, C-, or S-band $K_{dp} > 0.3°\,\text{km}^{-1}$ (and therefore also $Z_{dr} > 0.25\,\text{dB}$) were convective. This result implies that a C/S partitioning step, in addition to data quality thresholds, is most likely unnecessary when using $R(K_{dp})$ or $R(K_{dp}, \zeta_{dr})$ in the blended algorithm. The subset of data qualified for use in these relationships would nearly always be convective anyway.

2) RELATIONSHIPS BETWEEN VARIABLES

While convective DSDs generally had greater K_{dp} and C/S Z_{dr} ranges that overlapped, convective DSDs consistently exhibited higher K_{dp} (i.e., liquid water content) for a given Z_{dr} (i.e., diameter) than stratiform (Fig. 4). This behavior reflects the larger median drop sizes (i.e., larger Z_{dr}) but lower LWC (lower K_{dp}) in stratiform rain compared to convection over tropical oceans (T15). Since different C/S modes of $Z_{dr}(K_{dp})$ covariance exist (Fig. 4), different C/S $R(K_{dp}, \zeta_{dr})$ relationships could technically be motivated. However, most of the weak convection with $K_{dp} < 0.3°\,\text{km}^{-1}$ would not meet the $Z_{dr} > 0.25\,\text{dB}$ threshold and most stratiform rain did not meet the $K_{dp} > 0.3°\,\text{km}^{-1}$ threshold. Furthermore, Fig. 4 clearly illustrates that no data met the K_{dp} threshold but

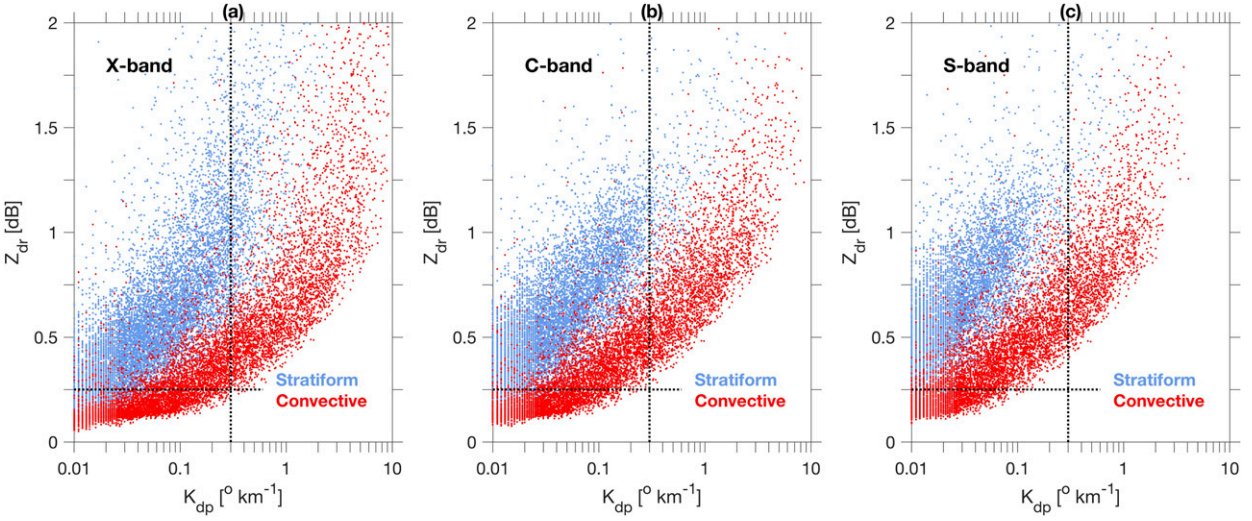

FIG. 4. Indo-Pacific warm pool DSD-simulated Z_{dr} and K_{dp} at (a) X, (b) C, and (c) S bands, colored by the T15 DSD-based C/S partitioning. Data quality thresholds of $Z_{dr} = 0.25\,\text{dB}$ and $K_{dp} = 0.3°\,\text{km}^{-1}$ are plotted for reference.

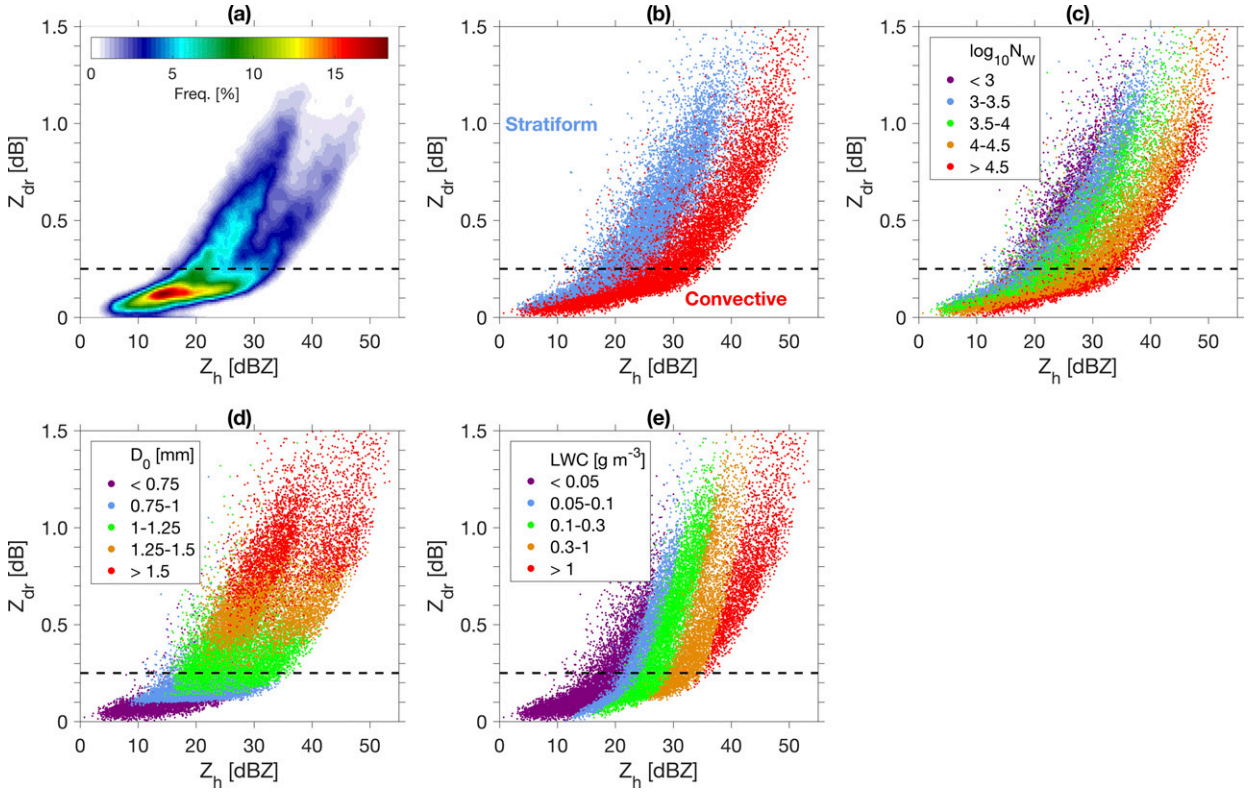

FIG. 5. Indo-Pacific warm pool DSD-simulated S-band Z_h and Z_{dr}: (a) 2D histogram contoured by frequency of occurrence, (b) DSD-based T15 C/S partitioning, and scatterplots colored by (c) normalized gamma DSD intercept parameter $\log_{10}N_W$, (d) D_0, and (e) LWC.

not the Z_{dr} threshold; that is, the surface-based disdrometer data do not indicate the presence of hail (C11) and also that tropical oceanic DSDs with sufficient LWC (0.1–1 g kg^{-1}) to produce $K_{dp} > 0.3^\circ$ km^{-1} are also always associated with $Z_{dr} > 0.25$ dB at each λ in this dataset. Therefore, for optimization rain algorithms deciding between estimators based on data quality thresholds, $R(K_{dp})$ is not needed and $R(K_{dp}, \zeta_{dr})$ would only be used during moderate-to-strong convective rain, while stratiform rain and weaker convection would be quantified by either $R(z)$ or $R(z, \zeta_{dr})$.

The Z_h versus Z_{dr} distribution shows two distinct modes of variability associated with either convective or stratiform rain (Fig. 5). A substantial portion of both C/S populations met the $Z_{dr} > 0.25$ dB threshold, which motivates a C/S option for $R(z, \zeta_{dr})$ (Fig. 5). The contoured density plot in Fig. 5a shows an overlapping, high-frequency-of-occurrence region below 20 dBZ and below 0.2 dB, respectively. As Z_h increases beyond about 20 dBZ, two modes of Z_{dr} variability emerge. Tropical maritime convection exhibited higher Z_h for a given Z_{dr} compared to stratiform rain (Fig. 5b). The C/S D_0 and D_{MAX} ranges overlap; however, stratiform rain has overall lower N_W and lower LWC (Figs. 5c–e; T15). While Z_{dr} is, to first order, dependent on D_0 (Fig. 2), Z_h depends on D and to a smaller extent $N(D)$. The number concentration N_W of drops is an order of magnitude higher in convection compared to stratiform, which can explain the higher Z_h for a given Z_{dr} (i.e., higher Z_h for a given D_0) in convection.

The tropical oceanic, combined convective and stratiform distribution of Z_h versus Z_{dr} in Fig. 5 is similar to that found over Kwajalein Atoll in the central Pacific (Bringi et al. 2011); Bonn, Germany (Borowska et al. 2011); Florida (Brandes et al. 2004), and over Oklahoma during tropical-like rain events (Ryzhkov et al. 2005b). In the current tropical oceanic dataset as well as in these aforementioned studies of weak-to-moderate convection, Z_{dr} remained below about 1 dB unless $Z_h >$ 30 dBZ.

In contrast to the tropical oceanic distribution in Fig. 5, a case study by Ryzhkov et al. (2005a) showed higher Z_{dr} for a given Z_h in stronger continental convection, some of which contained large hail (Gatlin et al. 2015). This continental convective distribution of Z_{dr} versus Z_h was characterized by $Z_{dr} > 1$ dB beginning

once $Z_h \sim 25$ dBZ. The value of Z_{dr} reached at least 2 dB by 45 dBZ, which is higher in magnitude than the entire tropical oceanic distribution in Fig. 5**.** Compared to open-ocean convection, continental convection is subject to more evaporation below higher cloud bases, which can deplete small drops and elevate the Z_{dr} (Kumjian and Ryzhkov 2010, 2012). Furthermore, continental convection contains stronger updrafts and more vigorous ice-based microphysical processes, leading to hail that can reach the ground and result in larger melted raindrops (May et al. 2002; Zipser 2003; Bringi et al. 2003; May and Keenan 2005; Cotton et al. 2011; Dolan et al. 2013; Gatlin et al. 2015; Schumacher et al. 2015; T15). For instance, convective DSD from Colorado hailstorms exhibited lower N_W with higher D_0 compared to tropical maritime rain N_W and D_0 ranges (Bringi et al. 2003; T15). Large raindrops, especially if few in number and not accompanied by numerous small drops, would produce large Z_h and large Z_{dr}. Therefore, differences between tropical oceanic versus continental convective cloud microphysical processes can explain the observed differences between their Z_h versus Z_{dr} distributions. Unlike convection, DSDs and dual-polarization radar variables during stratiform rain appear to exhibit more similar characteristics across different climate regimes (BC01; Bringi et al. 2003, 2009; Thurai et al. 2010; T15).

b. New dual-polarization rainfall relationships

Given the dependence and interdependence of dual-polarization radar variables on tropical oceanic DSD variability discussed in section 3a, this section explores new R relationships formed with these data [Table 1, updated tropical oceanic $R(z)$ estimators are repeated from T15]. The resulting C/S rain fraction estimate, the correlation coefficient r, the percent difference of total rain accumulation (i.e., the bias), and the root-mean-square error (RMSE) for each estimator are listed for each λ in Table 2. The C/S rain fractions varied by $\pm$(0%–2%) for each estimator depending on radar wavelength. Linear versions of Z_h, z (mm^6 m^{-3}), and Z_{dr}, ζ_{dr} (dimensionless) were used in regression equations because of their larger dynamic ranges. Data quality thresholds of $K_{dp} > 0.3°$ km^{-1} and $Z_{dr} > 0.25$ dB were implemented before deriving equations using each of these variables to avoid "overfitting" R relationships to noise and because higher correlation coefficients to 2DVD R were achieved by equations using these thresholds. Similarly, $R(A_h)$ and $R(A_h, \zeta_{dr})$ equations performed best when formed with data in which $Z_h >$ 20 dBZ. These equations are provided in Table 1. Ryzhkov and Zrnić (1995) and Bringi et al. (2012) also avoided overfitting R relationships by only performing regressions with data whose $R > 20$ or 10 mm h^{-1}.

TABLE 1. New tropical oceanic dual-polarization radar rainfall estimation equations at X, C, and S bands derived from the equatorial Indo-Pacific warm pool DSD and simulated radar variables: linear z (mm^6 m^{-3}), linear ζ_{dr} (unitless), K_{dp} (° km^{-1}), and A_h (dB m^{-1}). New $R(z)$ equations were derived from the same tropical oceanic dataset (T15) and are equivalent for the X, C, and S bands.

		X	C	S
$R(K_{dp}, \zeta_{dr}) = aK_{dp}^b \zeta_{dr}^c$				
All rain	a	28.13	45.70	96.57
All rain	b	0.92	0.88	0.93
All rain	c	−1.69	−1.67	−2.11
$R(z, \zeta_{dr}) = az\zeta_{dr}^c$				
All rain	a	0.0085	0.0086	0.0085
All rain	b	0.93	0.91	0.92
All rain	c	−4.46	−4.21	−5.24
Convective	a	0.014	0.017	0.015
Convective	b	0.86	0.82	0.84
Convective	c	−3.45	−2.90	−3.90
Stratiform	a	0.010	0.011	0.010
Stratiform	b	0.89	0.85	0.88
Stratiform	c	−4.075	−3.58	−4.57
$R(K_{dp}) = aK_{dp}^b$				
All rain	a	18.67	30.62	56.04
All rain	b	0.77	0.78	0.80
Convective	a	21.97	34.57	59.52
Convective	b	0.72	0.73	0.75
Stratiform	a	12.76	20.44	36.29
Stratiform	b	0.71	0.72	0.74
$R(A_h) = aA_h^b$				
All rain	a	69.54	447.37	3076.32
All rain	b	0.85	0.93	0.98
$R(A_h, \zeta_{dr}) = aA_h^b \zeta_{dr}^c$				
All rain	a	142.35	646.56	2684.09
All rain	b	0.95	0.97	0.97
All rain	c	−2.73	−1.40	0.36
$R(z) = az^b$ (from T15)				
All rain	a	0.0207	0.0207	0.0207
All rain	b	0.721	0.721	0.721
Convective	a	0.0366	0.0366	0.0366
Convective	b	0.684	0.684	0.684
Stratiform	a	0.0258	0.0258	0.0258
Stratiform	b	0.644	0.644	0.644

1) $R(K_{dp})$

The C/S $R(K_{dp})$ distributions at each λ illustrate that 77%, 86%, and 90% of X-, C-, and S-band data with $K_{dp} >$ 0.3° km^{-1} are convective (Fig. 6), which suggests that $R(K_{dp})$ does not require C/S partitioning in addition to a data quality threshold (also shown in Fig. 4). For instance, the convective and all-data equations (Table 1) and best-fit lines (Fig. 6) for $R(K_{dp})$ appear similar at all three λs above the $K_{dp} = 0.3°$ km^{-1} line since most samples above this level are convective. The $R(K_{dp})$ estimator based on data with $K_{dp} >$ 0.3° km^{-1} produced negligibly worse r results by 0.001 and negligibly worse RMSEs by 0.1 mm h^{-1}, so only the all-data $R(K_{dp})$ estimator was pursued further in this study.

TABLE 2. The X-, C-, and S-band comparisons between 2DVD rain rate and rain-rate estimators using DSD-simulated radar variables with and without C/S partitioning.

Methodology	λ	C/S rain fraction	r	Bias (%)	RMSE (mm h^{-1})
2DVD	—	81/19	—	—	—
$R(z)$	X	69/31	0.821	1.7	9.6
	C	70/30	0.899	7.1	6.0
	S	71/29	0.925	2.9	5.2
C/S $R(z)$	X	81/19	0.911	−2.9	7.1
	C	81/19	0.959	0.5	4.0
	S	82/18	0.967	−3.4	3.9
$R(K_{dp})$	X	74/26	0.985	6.9	2.7
	C	74/26	0.977	3.6	2.9
	S	75/25	0.980	1.8	2.7
C/S $R(K_{dp})$	X	81/19	0.990	1.6	1.9
	C	81/19	0.988	−0.3	2.0
	S	81/19	0.990	−0.7	1.9
$R(A_h)$	X	76/24	0.949	−6.1	5.6
	C	78/22	0.907	−5.4	7.4
	S	82/18	0.996	−0.6	1.2
$R(K_{dp}, \zeta_{dr})$	X	79/21	0.990	5.0	1.9
	C	78/22	0.993	3.4	1.6
	S	80/20	0.996	7.1	1.2
$R(z, \zeta_{dr})$	X	80/20	0.987	3.5	2.1
	C	79/21	0.989	4.8	2.0
	S	80/20	0.992	5.0	1.8
C/S $R(z, \zeta_{dr})$	X	81/19	0.989	2.5	1.9
	C	81/19	0.991	3.1	1.8
	S	81/19	0.994	3.3	1.5
$R(A_h, \zeta_{dr})$	X	80/20	0.996	−0.2	1.2
	C	81/19	0.990	−3.3	2.1
	S	81/19	0.994	3.1	1.7

Although only the convective $R(K_{dp})$ estimator would be used if a K_{dp} data quality threshold were employed, separate C/S $R(K_{dp})$ estimators were still formed. Compared to the all-data $R(K_{dp})$ estimator, the X-, C-, and S-band pair of C/S $R(K_{dp})$ estimators improved R accuracy (r = 0.988–0.990), yielded the same C/S rain fraction estimate as the 2DVD at all three λs, produced a substantially lower bias of −0.7% to 1.6%, and had a lower RMSE of 1.9–2.0 mm h^{-1} (Table 2). The exponents of the C/S $R(K_{dp})$ estimators (i.e., the slopes in log–log format in Figs. 6a–c) are nearly the same. However, of the two C/S estimators, the multiplicative coefficient (y intercepts in Figs. 6a–c) is higher for convective $R(K_{dp})$ since more LWC, higher N_W, and higher R are associated with the same K_{dp} in convective rain compared to stratiform rain (Figs. 6d–f).

2) $R(K_{dp}, \zeta_{dr})$ AND $R(Z, \zeta_{dr})$

While R is not very well correlated with Z_{dr} individually (r = 0.61), the $R(z, \zeta_{dr})$ and $R(K_{dp}, \zeta_{dr})$ estimators outperformed all individual $R(z)$ or $R(K_{dp})$ equations at each λ, including C/S formulations (Table 2). Errors and biases were lower for these multiparameter equations; however, their error structures were also more complicated because they are associated with two input parameters (Pepler et al. 2011; Pepler and May 2012). The ζ_{dr} coefficient in both multiparameter equations is negative to constrain the positive correlation of Z_h and K_{dp} to R (Table 1). The estimated C/S rain fractions by both of these multiparameter equations were within 1%–3% of the 2DVD C/S rain fraction at all three λs. The correlation coefficients between 2DVD R and R estimated from $R(K_{dp}, \zeta_{dr})$ and $R(z, \zeta_{dr})$ were high, between 0.992 and 0.996 at S band and slightly lower with decreasing λ. RMSEs between 2DVD R and R estimated by these multiparameter equations were also below 2 mm h^{-1} for all λs. Out of all of the K_{dp}-, Z_{dr}-, and Z_h-based estimators, the $R(K_{dp}, \zeta_{dr})$ equation performed best at each λ (Table 2). An interpretation of this result is

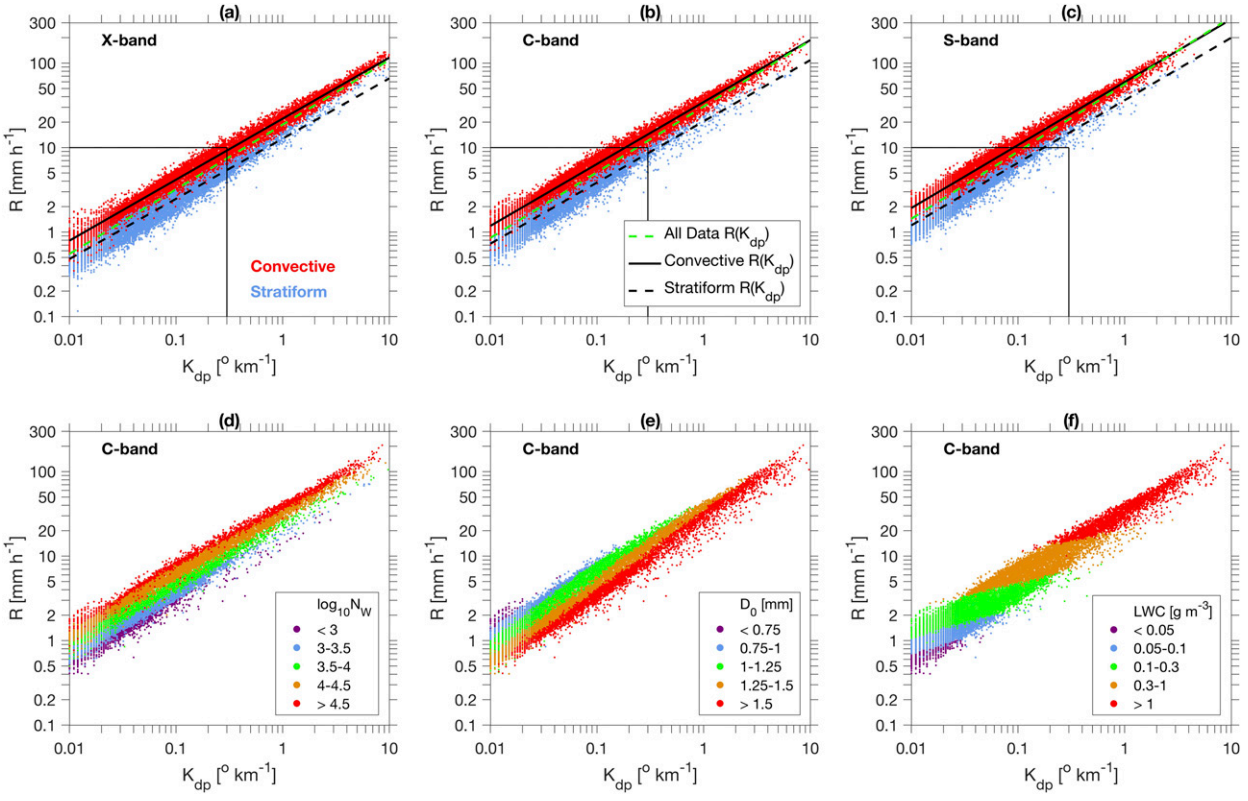

FIG. 6. Indo-Pacific warm pool DSD-simulated K_{dp} and measured R: (a) X-, (b) C-, and (c) S-band C/S distributions with best-fit lines (Table 1) and C-band distributions colored by the (d) normalized gamma intercept parameter $\log_{10}N_W$, (e) D_0, and (f) LWC.

that, of the K_{dp}-, Z_h-, and Z_{dr}-based estimators, the $R(K_{dp}, \zeta_{dr})$ equation most effectively accounted for tropical oceanic rain DSD variability.

Compared to the all-data $R(z, \zeta dr)$ estimator, the pair of C/S $R(z, \zeta_{dr})$ estimators offered only a 1% better C/S rain fraction (mirroring that of the 2DVD), 0.002 better r, 1%–1.5% lower bias, and 0.2–0.3 mm h^{-1} lower RMSE. As shown in Fig. 4, the $R(K_{dp}, Z_{dr})$ distribution only included convective data points once data quality thresholds were met for both variables. Therefore, C/S partitioning does not appear necessary or fruitful for the $R(K_{dp}, \zeta_{dr})$ or the $R(z, \zeta_{dr})$ estimators during tropical oceanic rain.

3) $R(A_h)$ AND $R(A_h, \zeta_{dr})$

For tropical oceanic rain, the accuracy of new $R(A_h)$ and $R(A_h, \zeta_{dr})$ estimators depended strongly on radar λ and only exceeded the accuracy of $R(K_{dp}, \zeta_{dr})$ at

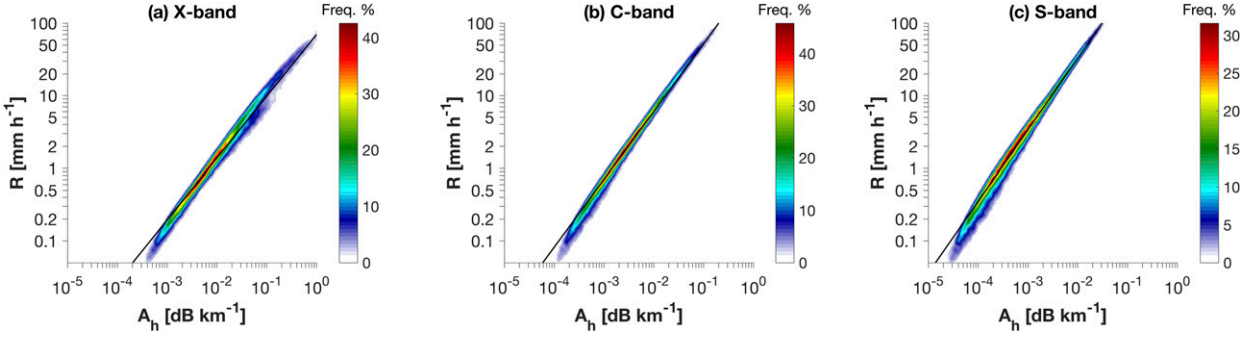

FIG. 7. Frequency of occurrence of Indo-Pacific warm pool DSD-simulated A_h and measured R at X, C, and S bands with best-fit lines from Table 1.

X band with the use of $R(A_h, \zeta_{dr})$ (Table 2). The $R(A_h)$ estimator performed as well as the top-ranking $R(K_{dp}, \zeta_{dr})$ estimator at S band, but was by far the lowest-ranking estimator of all dual-polarization options at the X and C bands in terms of r, bias, and RMSE. The underlying distribution of tropical oceanic $R(A_h)$ data points was most tightly clustered around the best-fit line at S band compared to shorter λ (Fig. 7), which was also noted by Ryzhkov et al. (2014). Unlike this theoretical analysis of tropical oceanic rain, previous studies focused on continental and coastal rain found that X- and C-band $R(A_h)$ estimators were actually able to outperform other dual-polarization R estimators based on z and K_{dp} once the measurement error, wet radome effects, beam blockage, and anomalous propagation were taken into account (Giangrande et al. 2014; Wang et al. 2014; Boodoo et al. 2015; Diederich et al. 2015a,b). Both $R(A_h)$ and $R(A_h, \zeta_{dr})$ performed even worse when separate C/S versions of these estimators were implemented at X, C, and S bands, meaning that C/S partitioning is neither necessary nor encouraged for either of the A_h-based estimators. Therefore, the theoretical utility of $R(A_h)$ and $R(A_h, \zeta_{dr})$ estimators over tropical oceans depended strongly on radar λ in that these estimators only offered significant skill at S band for $R(A_h)$ or at X band for $R(A_h, \zeta_{dr})$ and, even so, only the X-band $R(A_h, \zeta_{dr})$ estimator offered improved skill compared to X-band $R(K_{dp}, \zeta_{dr})$.

c. *Regional differences between rain estimators and their accuracy*

The coefficients and exponents of updated polarimetric equations for tropical oceanic rain in Table 1 were different from continental, subtropical, or coastal equations from other sources in the appendix (see Table A1) because the DSDs of tropical oceanic convection differ from that arising over continental or coastal locations (Bringi et al. 2003, 2009; Thurai et al. 2010; Wang et al. 2013, 2014; T15). The $R(K_{dp})$ coefficients were highest for the Wang et al. (2013) Taiwan typhoon estimator and new tropical oceanic all-data and convective $R(K_{dp})$ estimators, followed by coefficients from coastal equations and, then, the coefficients were lowest in continental estimators (Tables 1 and A1). These regional differences between $R(K_{dp})$ estimators reflect the fact that LWC is concentrated in generally smaller drops in the tropical oceanic rain regime (Wang et al. 2013; T15). The new tropical oceanic $R(K_{dp}, \zeta_{dr})$ equation coefficients and exponents were also highest, except at S band compared to estimators used by Brandes et al. (2002) for Florida coastal convection. Exponents and coefficients of the new tropical oceanic $R(A_h)$, $R(A_h, \zeta_{dr})$, and $R(z, \zeta_{dr})$ equations were within the same range as those derived from previous studies in other rain regimes.

The new R estimators fit to the tropical oceanic rain regime improved R estimation accuracy on this dataset compared to previously established continental or coastal R estimators at all λs (Tables 2, A1, and A2). When evaluated on this study's tropical oceanic simulated radar dataset, most of the previous equations from coastal and continental environments underestimated total R accumulation by double-digit percentages because tropical oceanic rain contains higher LWC for a given median raindrop diameter or drop oblateness. Equations from these coastal or continental rain regimes typically exhibited $r < 0.990$ and RMSE $> 3\,\text{mm}\,\text{h}^{-1}$. Notable exceptions were found for the X-, C-, and S-band $R(K_{dp}, \zeta_{dr})$ and $R(z, \zeta_{dr})$ equations formed from simulated DSDs by BC01; S-band $R(A_h)$ from Oklahoma by Ryzhkov et al. (2014); as well as $R(z, \zeta_{dr})$ formed by DSD data from the Kwajalein Atoll (Bringi et al. 2011), the latter of which is a location nearby that of the current dataset since both were collected in the western Pacific Ocean. Compared to measured 2DVD R, only these few aforementioned dual-polarization radar estimators were associated with $r \sim 0.992$–0.995, biases of only 5%–10%, and RMSEs $\leq 3\,\text{mm}\,\text{h}^{-1}$ (Table A1). The updated tropical oceanic $R(z)$ equations produced by T15 also outperformed other $R(z)$ methods used in other regions (Table A2). The $R(z)$ estimator used for tropical rain by the National Weather Service actually overestimated tropical oceanic rain by 37% and produced the lowest $r = 0.898$.

d. *Blended algorithm testing*

Based on results from previous subsections, the new tropical oceanic R estimators using K_{dp}, Z_{dr}, and Z_h were tested using the same logic as the liquid-only branch of the C11 CSU blended optimization algorithm with data quality thresholds of $Z_{dr} > 0.25\,\text{dB}$ and $K_{dp} > 0.3^\circ\,\text{km}^{-1}$ and without a Z_h threshold. According to this algorithm framework (see section 2), $R(z, \zeta_{dr})$ is used to calculate R if only the Z_{dr} threshold is met, $R(K_{dp})$ is used if only the K_{dp} threshold is met, $R(K_{dp}, \zeta_{dr})$ is used if both the Z_{dr} and K_{dp} thresholds are met simultaneously, and $R(z)$ is used if neither the K_{dp} nor the Z_{dr} thresholds is met. All four R estimators were updated for tropical oceanic rain using the DSD dataset discussed herein (Tables 1 and 2). T15 developed and tested the all-data and C/S versions of the tropical oceanic $R(z)$ estimators (Tables 1 and 2).

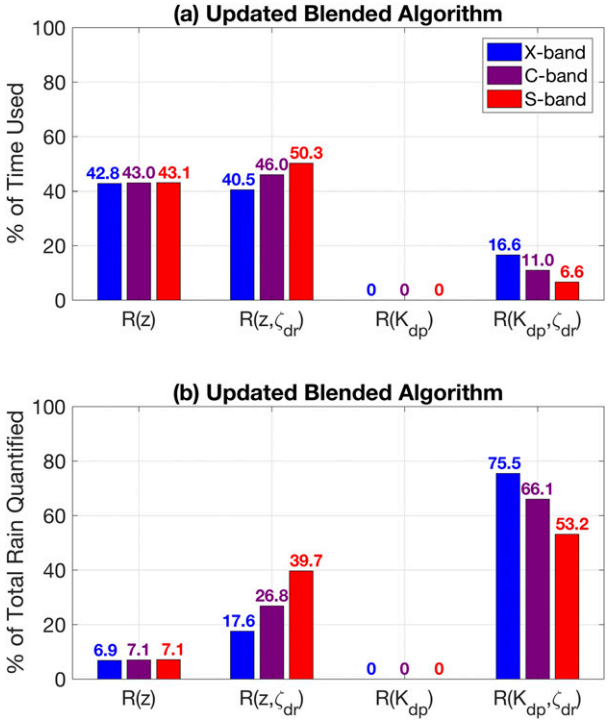

FIG. 8. Updated CSU blended rainfall algorithm performance over Indo-Pacific warm pool: (a) frequency at which each equation was used and (b) percentage of total rain quantified with each equation. New tropical oceanic R equations were used, including C/S $R(z)$ from T15. Percentages are listed above bars. In cases in which percentages differ by <0.5%, the same percentage is discussed for all λs within the text; e.g., $R(z)$ used 43% of the time on 7% of total rain at all three λs.

When implemented on this tropical oceanic dataset, the updated blended algorithm used either $R(z)$ or $R(z, \zeta_{dr})$ most often depending on λ, while the majority of the rain volume was always quantified by $R(K_{dp}, \zeta_{dr})$ (Fig. 8,[2] which mimics the C11 analysis). When Z_{dr} and K_{dp} were both below data quality thresholds, the blended algorithm defaulted to $R(z)$, which, at all three λs, occurred 43% of the time and for 7% of the total rain volume. At all three λs, 47% of these occurrences and 81% of this rain volume treated by $R(z)$ were convective. In cases where $Z_{dr} \geq 0.25$ dB but $K_{dp} < 0.3^\circ \text{km}^{-1}$, $R(z, \zeta_{dr})$ was used 40%, 46%, and 50% of the time at the X, C, and S bands. While 57% of data met the Z_{dr} threshold at all λs, only 17%, 11%, and 7% of the data met both the K_{dp} and the Z_{dr} thresholds at the X, C, and S bands. This led the updated blended algorithm to use $R(K_{dp}, \zeta_{dr})$ only 17%, 11%, and 7% of the time at X, C, and S bands, which explains why $R(z, \zeta_{dr})$ was used least frequently at X band. There were no times when X-, C-, or S-band K_{dp} results were greater than 0.3°km^{-1} and Z_{dr} was less than 0.25 dB in this tropical oceanic DSD dataset (Fig. 4). This implies that no hail was observed in this tropical oceanic surface disdrometer dataset and also that tropical oceanic DSDs with sufficient LWC ($0.1–1\ \text{g kg}^{-1}$) to produce $K_{dp} > 0.3^\circ \text{km}^{-1}$ are also always associated with $Z_{dr} > 0.25$ dB at each λ in this dataset (Figs. 1 and 2). Therefore, as expected from previous subsections, $R(K_{dp})$ was unused in the blended algorithm at any λ. Since $R(K_{dp}, \zeta_{dr})$ tended to be used during higher-R situations according to the algorithm's design, this equation quantified the most rainfall (76%, 66%, and 53% at X, C, and S bands) even though it was used least often (17%, 11%, and 7% of the dataset at X, C, and S bands).

Even without C/S partitioning of any equations, the blended algorithm produced higher r, lower percent error, and lower RMSEs (Table 3) compared to any of the individual equations it contained at all three λs (Table 2). This implies that the blended algorithm is more accurate than any of its individual parts. Blended algorithm accuracy was only exceeded by that of $R(A_h)$ at X band (Table 2). Blended algorithm accuracy improved slightly at all λs when C/S $R(z)$ equations were used because the C/S versions of the $R(z)$ equations had a higher goodness of fit than the $R(z)$ fit to all data (Tables 2 and 3) and because these $R(z)$ equations were used 43% of the time on 7% of the total rain at all three λs. The population treated by $R(z)$ was made up of 47% convective rain in terms of occurrences and 81% convective rain in terms of volume. With C/S $R(z)$ equations, the blended algorithm's bias decreased by 1.6%, the RMSE decreased by $0.1\ \text{mm h}^{-1}$, r remained the same or increased by 0.001, and the C/S fraction estimate improved by 1% at all three λs.

The potential benefit of using separate C/S $R(z)$ equations in the blended algorithm was overshadowed by higher-magnitude errors in a test with these equations but with an incorrect C/S classification (Table 3). When a continental partitioning method between convective and stratiform rain was used (Bringi et al. 2003, 2009), the errors and biases grew roughly 3 times greater in magnitude compared to the decreases in errors and biases brought about by C/S $R(z)$: r decreased by 0.003 at X and S bands or by 0.016 at C band, the total rain estimate bias increased by 7%–13%, RMSE increased by $1.4–0.6\ \text{mm h}^{-1}$ at C and S bands (RMSE decreased by $0.2\ \text{mm h}^{-1}$ at X band), and the C/S fraction became offset by 8% at X and S bands or 2% at C band compared to the 2DVD observations (Table 3). Therefore, C/S $R(z)$ equations should only be applied

[2] In cases where percentages listed in Fig. 8 differ by less than 0.5%, the same percentage is discussed for all λs within the text; e.g., $R(z)$ is used 43% of the time on 7% of total rain at all λs.

TABLE 3. The C/S rain fraction, correlation coefficient r, percentage difference of total rain (bias), and RMSE of X-, C-, and S-band blended algorithm results updated with new equations compared to 2DVD R. The 2DVD-estimated C/S fraction = 81/19; see Table 2. The C/S partitioning is performed with T15's $\log_{10}N_W$ method unless otherwise noted.

	C/S rain fraction	r	Bias (%)	RMSE (mm h^{-1})
Updated X-band blended algorithm tests				
No C/S equations	79/21	0.990	3.7	1.9
C/S $R(z)$	80/20	0.991	2.1	1.8
C/S $R(z)$ and C/S $R(z, \zeta_{dr})$	81/19	0.991	2.2	1.8
C/S $R(z)$ with Bringi et al. (2009) C/S classification	73/27	0.987	9.5	1.6
Updated C-band blended algorithm tests				
No C/S equations	78/22	0.993	3.8	1.6
C/S $R(z)$	79/21	0.993	2.2	1.5
C/S $R(z)$ and $R(z, \zeta_{dr})$	80/20	0.994	2.0	1.5
C/S $R(z)$ with Bringi et al. (2009) C/S classification	79/21	0.978	14.9	2.9
Updated S-band blended algorithm tests				
No C/S equations	79/21	0.997	3.4	1.1
C/S $R(z)$	80/20	0.997	1.8	1.0
C/S $R(z)$ and $R(z, \zeta_{dr})$	81/19	0.997	1.4	1.0
C/S $R(z)$ with Bringi et al. (2009) C/S classification	73/27	0.994	9.5	1.6

when the C/S partitioning method can confidently distinguish between radar echoes or DSD samples for a particular rain regime (Steiner et al. 1995; Yuter and Houze 1998; Schumacher and Houze 2003; Powell et al. 2016; T15; Table 3).

Negligible further improvement to blended algorithm performance was gained when C/S $R(z, \zeta_{dr})$ equations were used compared to when the only C/S option was for $R(z)$: 0–0.001 r change, 0.0%–0.4% lower bias, no RMSE decrease, and 1% better C/S rain fraction at all three λs (Table 3). Based on these results, C/S $R(z, \zeta_{dr})$ equations do not seem warranted or necessary given the larger uncertainty involved in implementing the C/S equations (T15; Powell et al. 2016; Table 3).

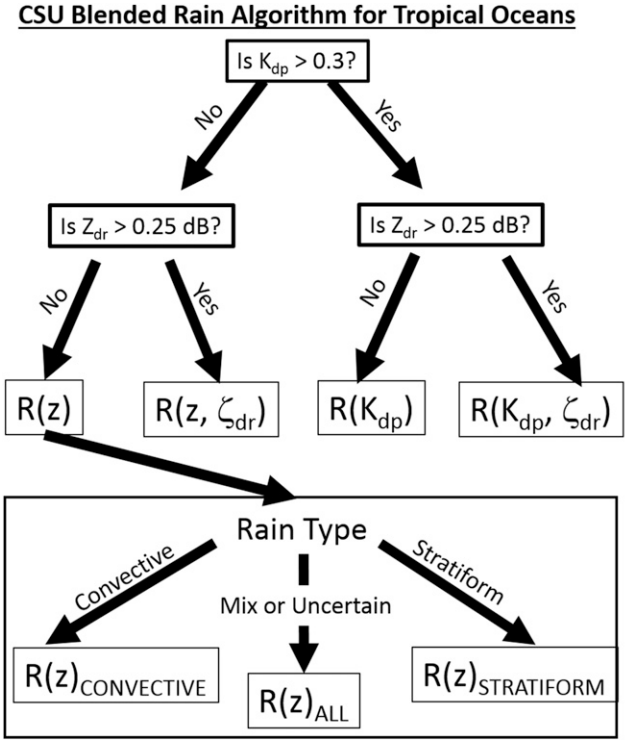

λ	X-band	C-band	S-band
$R(K_{dp}, \zeta_{dr}) = a\ K_{dp}^{\ b}\ \zeta_{dr}^{\ c}$			
a	28.13	45.70	96.57
b	0.92	0.88	0.93
c	-1.69	-1.67	-2.11
$R(z, \zeta_{dr}) = a\ z^b\ \zeta_{dr}^{\ c}$			
a	0.0085	0.0086	0.0085
b	0.93	0.91	0.92
c	-4.46	-4.21	-5.24
$R(K_{dp}) = a\ K_{dp}^{\ b}$			
a	18.67	30.62	56.04
b	0.77	0.78	0.80
$R(z) = a\ z^b$			
a ALL DATA			0.021
b ALL DATA			0.72
a CONVECTIVE			0.037
b CONVECTIVE			0.68
a STRATIFORM			0.026
b STRATIFORM			0.64

FIG. 9. CSU blended rain algorithm framework updated for dual-polarization radar rainfall estimation over tropical oceans.

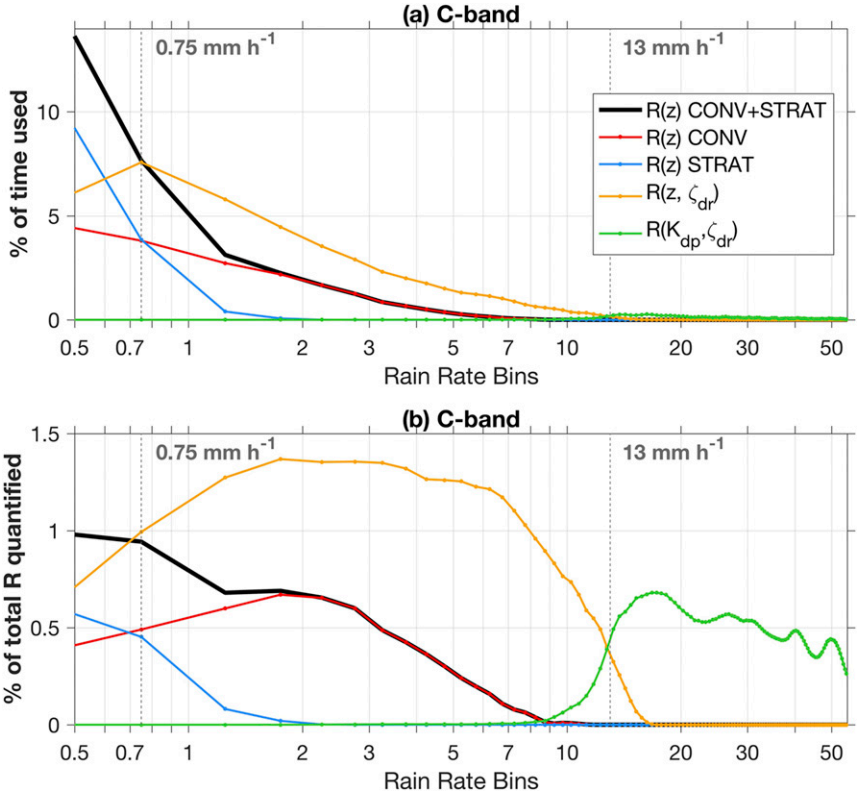

FIG. 10. (a) How often each equation was used and (b) how much total rain was quantified by each equation in the updated blended algorithm for tropical oceanic rain at C band. The only significant difference between each λ is that, at the X, C, and S bands, $R(K_{dp}, \zeta_{dr})$ begins to dominate the R estimation once $R > 8$, 13, and 22 mm h^{-1}, respectively. Normalized histogram bin widths = 0.5 mm h^{-1}.

4. Discussion

a. Updated blended algorithm

The results in section 3 motivate our desire to update the blended algorithm according to Fig. 9 for dual-polarization radar rainfall estimation over tropical oceans. When implemented in this way, C/S $R(z)$ relationships are only used when $R < 7$ mm h^{-1} at all three λs (Fig. 10 for C band). These $R(z)$ equations account for over half of the total rain when $R < 3$ mm h^{-1} and the majority of rain when $R < 0.7$ mm h^{-1}. For perspective, rain rates below 7, 3, and 0.7 mm h^{-1} make up only 23%, 11%, and 2% of the total rain volume, but 82%, 67%, and 33% of rain occurrences. Since $R(z, \zeta_{dr})$ becomes more commonly used between 0.7 and 7 mm h^{-1}, the total percentage of rainfall attributable to $R(z)$ levels out to 43% at three λs in terms of frequency, but yet just 7% of the rain volume. In terms of both frequency and rain volume, $R(K_{dp}, \zeta_{dr})$ dominates once R exceeds 8, 13, and 22 mm h^{-1} at X, C, and S bands. Therefore, the blended algorithm sequesters errors associated with C/S $R(z)$ equations to the lightly raining population, where $Z_{dr} < 0.25$ dB, 96% of which occurs from $R < 5$ mm h^{-1} in terms of frequency and 84% of which occurs from $R < 2$ mm h^{-1}.

It could be considered ironic that a dual-polarization radar would still rely on $R(z)$ 43% of the time, which amounts to 7% of the total rain (47% of these occurrences and 81% of this rain volume were convective at all λs). In the remaining 57% of rain occurrences and 93% of rain volume where $Z_{dr} > 0.25$ and/or $K_{dp} > 0.3°$ km^{-1}, dual-polarization R estimators improve rainfall estimation accuracy and eliminate the need for C/S partitioning (Fig. 9). All-data versions of $R(K_{dp})$, $R(z, \zeta_{dr})$, and $R(K_{dp}, \zeta_{dr})$, without C/S partitioning, appear in the recommended version of the blended algorithm for tropical oceanic rain (Fig. 9). Since $R(z, \zeta_{dr})$ and $R(K_{dp}, \zeta_{dr})$ are more accurate than C/S $R(z)$, it is therefore unsurprising that the X-, C-, and S-band implementations of the blended algorithm exhibited 0.03–0.08 higher r and 3–5 mm h^{-1} lower RMSE values compared to the C/S $R(z)$ treatment of this dataset (Tables 2 and 3).

TABLE 4. Correlation coefficient r of Indo-Pacific warm pool 2DVD rainfall to rainfall estimated from new equations with and without C/S partitioning at X, C, and S bands.

Equation type	X-band r	C-band r	S-band r	Δr from X to S band
$R(z)$	0.822	0.899	0.925	+0.103
C/S $R(z)$	0.911	0.959	0.967	+0.056
$R(K_{dp})$	0.985	0.977	0.980	−0.005
$R(A_h)$	0.949	0.907	0.996	+0.047
$R(z, \zeta_{dr})$	0.987	0.989	0.992	+0.005
$R(K_{dp}, \zeta_{dr})$	0.990	0.993	0.996	+0.006
$R(A_h, \zeta_{dr})$	0.996	0.990	0.994	−0.002
Updated blended algorithm with C/S $R(z)$	0.991	0.993	0.997	+0.006
Improvement of blended algorithm over C/S $R(z)$	+0.080	+0.034	+0.030	+0.05

Increasing the reliability of Z_{dr} and K_{dp} measurements could further improve tropical oceanic R estimation. Errors due to $R(z)$ and C/S partitioning could be reduced if Z_{dr} and K_{dp} could be used at lower magnitudes. These errors are currently sequestered to lightly raining time periods ($R < 7\,\text{mm h}^{-1}$), whereas the majority of rain accumulation is produced by higher rain rates that are accounted for by more accurate dual-polarization R estimators (Figs. 8 and 10), The usable portion of dual-polarization radar data could also be maximized by reducing the amount of data compromised by sea spray scattering, sea surface clutter, attenuation, and velocity aliasing (BC01; Nguyen et al. 2008).

b. *Wavelength dependence*

Dual-polarization radar rainfall estimation improves upon $R(z)$-based methods over tropical oceans at the X, C, and S bands (Tables 2 and 4), and updated R estimators based on tropical oceanic DSD also improve R estimation accuracy in this region (Tables 2, A1, and A2). Using updated S-band equations, r improved from 0.967 for C/S $R(z)$ equations to 0.997 for the blended algorithm, 0.996 for $R(K_{dp}, \zeta_{dr})$, and 0.992 for $R(z, \zeta_{dr})$.

Dual-polarization radar R methods consistently performed best at S band in terms of r, bias, and RMSE (Tables 2–4), which is most likely due to the higher occurrence of non-Rayleigh scattering at shorter λ. The value of r changed by −0.003 from S to C band and by from −0.005 to −0.006 from S to X band for $R(z, \zeta_{dr})$ and $R(K_{dp}, \zeta_{dr})$. The blended algorithm r changed by −0.004 from S to C band and changed by −0.006 from S to X band. Even so, the blended algorithm still outperformed all of its individual component equations at all λs. Additionally, blended algorithm accuracy degradation at shorter λs was still 5–13 times smaller than the improved accuracy gained by using dual-polarization radar variables compared to single-polarization methods: r changed by +0.080, +0.034, and +0.030 for X-, C-, and S-band dual-polarization methods compared to C/S $R(z)$, while r changed by only −0.006 from S- to X-band blended algorithm differences.

From S to X band, C/S $R(z)$ accuracy actually degraded by an even larger margin (r changed by −0.056) compared to that of the blended algorithm. The Z_h, Z_{dr}, and K_{dp} results were all impacted by non-Rayleigh scattering, but $R(z)$ was apparently more vulnerable to these effects than a blended combination of all four equations. Therefore, the blended algorithm displayed a greater potential to improve R accuracy over C/S $R(z)$ estimators at shorter λs (Table 4): r changed by +0.080, +0.034, and +0.030 between C/S $R(z)$ and the blended algorithm at X, C, and S bands.

Maximum drop diameters observed in this tropical oceanic rain regime were usually below 5 mm (Fig. 2; T15), which is, for the most part, below the Rayleigh drop diameter threshold found by Zrnić et al. (2000) and Carey and Petersen (2015): 5 mm at C band and 3 mm at X band. However, tropical convective DSDs contain significant LWC even when drop diameters remain small (Figs. 1 and 2; T15), so radar signal attenuation still occurs at the C and X bands in this regime. Resonance effects are also possible at C band. For instance, r for $R(K_{dp})$ actually decreased by 0.003 from S to C band, and then r increased again by 0.005 from C to X band (Zrnić et al. 2000; Keenan et al. 2001).

c. *Other sources of error*

This study focuses on sources of error in dual-polarization radar rainfall estimation caused by DSD variability intrinsic to the tropical oceanic rain regime, but does not address the practical implementation of radar-based R estimation. We do not address other known sources of error related to radar measurement collection or processing, such as wet radomes, Z_{dr} calibration, K_{dp} filtering, A_h estimation from Φ_{dp} and z, partial beam blockage, attenuation and differential attenuation, radar-based C/S radar partitioning, or non-meteorological echo, such as by sea spray (e.g., BC01). These sources of error should be addressed by future

studies regarding dual-polarization radar R estimation over tropical oceans, but this is beyond the scope of the current study.

5. Conclusions

Dual-polarization radar rainfall estimation relationships have been tested almost entirely in continental and subtropical coastal rain. Prior to this study it was unclear how dual-polarization rainfall estimation performed over the tropical oceans, where the majority of rain occurs. A 1.5-yr Indo-Pacific warm pool disdrometer dataset was used to quantify the impacts of tropical oceanic DSD variability on K_{dp}, Z_{dr}, A_h, and Z_h, as well as their resulting utility for dual-polarization radar rainfall (R) estimation. The linear versions of differential reflectivity ζ and reflectivity z were used.

Radar variables simulated from DSD accounted for the high LWC of tropical oceanic convective rain, as well as the propensity for Z_{dr} to be lower for a given Z_h and K_{dp} in convection compared to stratiform rain in this regime. Dual-polarization radar variables were overall lower in tropical oceanic convection compared to continental or subtropical coastal convection, the latter of which tends to be characterized by larger drop sizes and lower number concentrations. New $R(z, \zeta_{dr})$, $R(K_{dp})$, $R(K_{dp}, \zeta_{dr})$, $R(A_h)$, and $R(A_h, \zeta_{dr})$ equations were formed to account for tropical oceanic DSD variability at the X, C, and S bands. Compared to R estimators formed from other continental and coastal regions, the new tropical oceanic R estimators always performed best at all wavelengths (λs) tested. At each λ, $R(K_{dp}, \zeta_{dr})$ consistently outperformed $R(z, \zeta_{dr})$ and the latter outperformed $R(K_{dp})$. The new $R(A_h)$ estimator only displayed skill at S band and, even then, did not exceed the accuracy of $R(K_{dp}, Z_{dr})$ at this λ. The $R(A_h, \zeta_{dr})$ estimator only exceeded the accuracy of $R(K_{dp}, Z_{dr})$ at X band.

The CSU blended algorithm was updated for estimating rainfall over tropical oceans by incorporating new tropical oceanic R estimators based on Z_h, Z_{dr}, and K_{dp} and also by lowering the Z_{dr} data quality threshold compared to its original implementation by C11 over the continental United States. The updated tropical oceanic blended rain algorithm uses thresholds of $Z_{dr} > 0.25$ dB and $K_{dp} > 0.3^\circ \text{km}^{-1}$ to access R relationships with either or both of those variables; otherwise it defaults to $R(z)$.

Tropical oceanic DSD with $K_{dp} > 0.3^\circ \text{km}^{-1}$ also exhibited $Z_{dr} > 0.25$ dB at all three radar λs, so $R(K_{dp})$ was never called upon by the updated blended algorithm in this rain regime. Lowering the K_{dp} threshold further did not change this behavior. In previous studies over continents and coasts, the $R(K_{dp})$ branch of the blended algorithm has been utilized for rain with low Z_{dr} but high K_{dp} (C11). We hypothesize that $R(K_{dp})$ is not utilized over tropical oceans because hail does not reach the surface in this regime and because tropical oceanic DSDs with enough LWC to produce $K_{dp} > 0.3^\circ \text{km}^{-1}$ also always produce $Z_{dr} > 0.25$ dB.

Since K_{dp} and Z_{dr} were both overall lower in magnitude within the tropical oceanic rain regime compared to continental rain, $R(z)$ was still used by the blended algorithm 43% of the time on 7% of total rain at X, C, and S bands. Out of these occurrences, 47% were convective, 96% involved $R < 5 \text{ mm h}^{-1}$, and 84% were associated with $R < 2 \text{ mm h}^{-1}$. Since weak convection and stratiform rain overlap at these low rain rates, partitioning between C/S $R(z)$ estimators helped improve the blended algorithm's performance and are thus recommended where confident radar echo partitioning is possible.

At all three λs, $R(z)$ was used when R was between 0 and 7 mm h^{-1}, $R(z, \zeta_{dr})$ became the most commonly used estimator and quantified the most rain volume as R increased above 0.7 mm h^{-1}, and $R(K_{dp}, \zeta_{dr})$ became both the most commonly used and quantified the most rain at $R > 8$, 13, and 22 mm h^{-1} at the X, C, and S bands. The C/S partitioning was unnecessary for $R(K_{dp}, \zeta_{dr})$, $R(z, \zeta_{dr})$, and $R(K_{dp})$ because $R(K_{dp}, \zeta_{dr})$ was used almost exclusively in convective rain, C/S $R(z, \zeta_{dr})$ equations did not significantly improve the blended algorithm accuracy, and $R(K_{dp})$ was never used. Therefore, dual-polarization technology helped sequester errors associated with C/S partitioning and $R(z)$ to $R < 7 \text{ mm h}^{-1}$, such that C/S $R(z)$ only accounted for more than half the rain volume when $R < 3 \text{ mm h}^{-1}$.

Between X-, C-, and S-band wavelengths, $R(z, \zeta_{dr})$ quantified between 40%, 45%, and 50% of the total rain accumulation and $R(K_{dp}, \zeta_{dr})$ quantified 53%, 63%, and 74% of the total rain accumulation. Since $R(K_{dp}, \zeta_{dr})$ was more accurate than $R(z, \zeta_{dr})$, and both were more accurate than C/S $R(z)$, the blended algorithm capitalized on the strengths of each relationship by using more accurate relationships more often. As a result, the blended algorithm was more accurate than any of its component equations.

Dual-polarization radar R estimation techniques were increasingly more accurate than single-polarization $R(z)$ estimators at shorter λs. We found that K_{dp} could be used in the blended algorithm more frequently at shorter λs, $R(K_{dp}, \zeta_{dr})$ was more accurate than $R(z, \zeta_{dr})$, and both equations were far more accurate than $R(z)$. All R estimators were slightly less accurate at shorter λ due to non-Rayleigh scattering, but an

TABLE A1. Previously established dual-polarization radar rainfall estimators at X, C, and S bands. The correlation coefficient r, percent difference in total rain accumulation (bias; %), and RMSE (mm h^{-1}) were calculated between 2DVD R and R estimated with simulated radar variables.

λ		Source	r	Bias (%)	RMSE
		$R(K_{dp}, \zeta_{dr})$			
X	$R = 28.6 \times K_{dp}^{0.950} \zeta_{dr}^{-1.37}$	BC01; simulated DSD	0.993	4.21	2.48
C	$R = 37.9 \times K_{dp}^{0.890} \zeta_{dr}^{-0.72}$	BC01; simulated DSD	0.987	−3.71	2.42
	$R = 64.4 \times K_{dp}^{0.952} \zeta_{dr}^{-2.77}$	Keenan et al. (2001); Darwin, Australia	0.990	18.26	2.57
S	$R = 90.8 \times K_{dp}^{0.930} \zeta_{dr}^{-1.69}$	BC01; simulated DSD	0.995	−4.50	1.40
	$R = 63.3 \times K_{dp}^{0.851} \zeta_{dr}^{-0.72}$	Ryzhkov et al. (2005a); Bringi shape, OK	0.990	−10.78	2.18
	$R = 136.0 \times K_{dp}^{0.968} \zeta_{dr}^{-2.86}$	Brandes et al. (2002); FL	0.994	8.81	2.66
		$R(z, \zeta_{dr})$			
X	$R = 0.0039 \times z^{1.07} \zeta_{dr}^{-5.97}$	BC01; simulated DSD	0.984	19.79	5.11
C	$R = 0.01210 \times z^{0.82} \zeta_{dr}^{-1.75}$	Bringi et al. (2011); Chilbolten, United Kingdom	0.985	−3.79	2.26
	$R = 0.00580 \times z^{0.91} \zeta_{dr}^{-2.09}$	BC01; simulated DSD	0.984	−1.04	3.11
	$R = 0.00870 \times z^{0.91} \zeta_{dr}^{-4.94}$	Keenan et al. (2001); Darwin	0.983	18.26	3.41
S	$R = 0.0067 \times z^{0.927} \zeta_{dr}^{-3.43}$	BC01; simulated DSD	0.992	9.59	3.45
	$R = 0.0142 \times z^{0.770} \zeta_{dr}^{-1.67}$	Ryzhkov et al. (2005a); equilibrium shape, OK	0.978	−25.27	4.56
	$R = 0.0110 \times z^{0.850} \zeta_{dr}^{-3.28}$	Bringi et al. (2012); Kwajalein Atoll, west Pacific	0.994	−10.72	2.16
	$R = 0.00746 \times z^{0.945} \zeta_{dr}^{-4.76}$	Brandes et al. (2002); FL	0.995	11.69	2.77
		$R(A_h, \zeta_{dr})$			
X	$R = 155.6 \times A_h \zeta_{dr}^{-1.97}$	Thurai et al. (2017); IA	0.993	−17.45	5.76
C	$R = 874 \times A_h^{1.008} \zeta_{dr}^{-3.01}$	Keenan et al. (2001); Darwin	0.991	11.12	2.43
		$R(K_{dp})$			
X	$R = 16.90 \times K_{dp}^{0.801}$	Park et al. (2005); OK	0.986	−15.65	3.06
	$R = 15.00 \times K_{dp}^{0.760}$	Matrosov et al. (2006); CO	0.985	−24.73	4.59
C	$R = 31.37 \times K_{dp}^{0.835}$	Keenan et al. (2001); Darwin	0.974	−4.59	3.14
	$R = 24.68 \times K_{dp}^{0.810}$	Bringi et al. (2011); Chilbolten	0.975	−23.85	3.99
	$R = 28.80 \times K_{dp}^{0.850}$	Bringi et al. (2006); Okinawa, Japan	0.973	−13.09	3.16
	$R = 25.10 \times K_{dp}^{0.777}$	Gu et al. (2011); OK	0.977	−20.45	4.03
	$R = 34.60 \times K_{dp}^{0.830}$	Keenan et al. (2001); Darwin	0.974	5.52	3.72
	$R = 35.40 \times K_{dp}^{0.799}$	Wang et al. (2013); Taiwan typhoon	0.976	9.99	3.58
	$R = 31.37 \times K_{dp}^{0.835}$	Keenan et al. (2001); Darwin	0.974	−4.81	3.14
	$R = 22.15 \times K_{dp}^{0.866}$	Zrnić et al. (2000, scaled from S-band version: Sachidananda and Zrnić (1987)	0.971	−33.67	4.63
S	$R = 50.70 \times K_{dp}^{0.850}$	BC01; simulated	0.977	−17.20	3.11
	$R = 54.30 \times K_{dp}^{0.806}$	Brandes et al. (2002); FL	0.979	−6.08	2.70
	$R = 51.60 \times K_{dp}^{0.710}$	Illingworth and Blackman (2002); simulated	0.979	3.12	2.92
	$R = 50.30 \times K_{dp}^{0.812}$	Ryzhkov et al. (2005a); Bringi shape, OK	0.979	−13.70	3.03
	$R = 41.00 \times K_{dp}^{0.750}$	Matrosov et al. (2006) CO	0.980	−23.11	4.57
	$R = 40.60 \times K_{dp}^{0.866}$	Sachidananda and Zrnić (1987)	0.976	−34.98	4.78
	$R = 40.50 \times K_{dp}^{0.850}$	Chandrasekar et al. (1990); OK	0.977	−33.86	4.77
		$R(A_h)$			
X	$R = 43.5 \times A_h^{0.79}$	Giangrande et al. (2014) and Diederich et al. (2015a) at 20°C; OK	0.958	37.60	4.91
C	$R = 294 \times A_h^{0.89}$	Giangrande et al. (2014) and Diederich et al. (2015a) at 20°C; OK	0.920	24.46	5.30
	$R = 359 \times A_h^{0.88}$	Wang et al. (2014); Taiwan typhoon	0.923	−1.42	5.61
S	$R = 4120 \times A_h^{1.03}$	Ryzhkov et al. (2014); OK	0.995	−7.21	2.55

order-of-magnitude-greater degradation of accuracy occurred due to the use of $R(z)$. The benefit of dual-polarization technology for rainfall estimation [r changes of +0.080, +0.034, and +0.030 from C/S $R(z)$ to the blended algorithm at X, C, and S bands] greatly outweighed the degradation in blended algorithm accuracy from S to X band caused by non-Rayleigh scattering (r changed by −0.006). For example, the X-band blended algorithm still outperformed S-band C/S $R(z)$ equations. This comparison shows that dual-polarization radars are worthwhile to pursue at all wavelengths over tropical oceans.

Acknowledgments. This research was funded with aid from EJT's NSF Graduate Research Fellowship Award (DGE-1321845) and postdoctoral research support from the Applied Physics Laboratory at the University of Washington, NSF Award AGS-1063928 (SAR), as

TABLE A2. Previously established single-polarization radar rainfall estimators, which are independent of radar λ. Correlation coefficient *r*, percent difference in total rain accumulation (bias), and RMSE (mm h^{-1}) were calculated between 2DVD *R* and *R* estimated with simulated S-band radar variables.

λ	$R(z)$ and $z(R)$	Source	*r*	Bias (%)	RMSE
X/C/S	$R = 0.0366 \times z^{0.684}$ $z = 126 \times R^{1.44}$	T15; tropical oceanic, convective rain	0.967	−3.38	3.89
	$R = 0.0258 \times z^{0.644}$ $z = 291 \times R^{1.55}$	T15; tropical oceanic, stratiform rain	0.967	−3.38	3.89
	$R = 0.0207 \times z^{0.721}$ $z = 216 \times R^{1.39}$	T15; tropical oceanic, all rain	0.925	2.85	5.20
	$R = 0.0274 \times z^{0.694}$ $z = 178 \times R^{1.44}$	Yoneyama et al. (2008); tropical Indian Ocean	0.930	0.04	4.94
	$R = 0.0170 \times z^{0.833}$ $z = 300 \times R^{1.40}$	NWS; continental convection, United States	0.927	−25.38	5.52
	$R = 0.0100 \times z^{0.833}$ $z = 250 \times R^{1.20}$	NWS; tropical United States	0.898	37.65	13.64
	$R = 0.0877 \times z^{0.500}$ $z = 130 \times R^{2.00}$	NWS cool season eastern United States	0.935	−43.36	9.29
	$R = 0.0365 \times z^{0.625}$ $z = 200 \times R^{1.66}$	NWS stratiform, Marshall and Palmer (1948); Canada	0.938	−29.46	6.55

well as DOE/ASR Awards DE-SC7016 (SAR, BD) and DE-SC8583 (VC), and NASA's Precipitation Measurement Mission Awards NNX16AD85G (SAR, BD), NNX16AE26G (VC), and NNX16AD47G (MT). We acknowledge DOE/ARM for supplying the long-term Manus and Gan Islands 2DVD dataset. Thanks are given to Paul Hein and G. J. Huang for data management and processing (both CSU). We appreciate conversations with Scott Collis (Argonne National Laboratory) and Christopher Williams (CIRES), as well as Douglas C. Stolz, John M. Peters, Elizabeth Barnes, and Scott Powell (all CSU). We are also particularly grateful to V. N. Bringi (CSU) for his insightful comments regarding this work. We thank Michael Dixon, John Hubbert, Bob Rilling, and Scott Ellis (NCAR/EOL) for discussions concerning DYNAMO S-Pol radar data and analysis. We also thank Chidong Zhang, Kunio Yoneyama, and Chuck Long for their leadership in the DYNAMO/CINDY/AMIE projects, respectively. Suggestions from three anonymous reviewers and the editor led to improvements of this paper.

APPENDIX

Previously Established *R* Relations

Previously established relations for *R* estimation using K_{dp}, Z_{dr}, Z_h, and A_h at X, C, and S band are contained in Tables A1 and A2. For each estimator, the correlation coefficient *r*, percent difference of total rain (i.e., bias), and RMSE were computed using tropical oceanic radar variables simulated in the current study compared to measured tropical oceanic 2DVD *R*. The tropical oceanic *R* estimators developed in the current study (Table 1) always outperformed the previously established estimators from other regions shown in Tables A1 and A2 at each λ (Table 2).

REFERENCES

Aydin, K., and V. Giridhar, 1992: C-band dual-polarization radar observables in rain. *J. Atmos. Oceanic Technol.*, **9**, 383–390, https://doi.org/10.1175/1520-0426(1992)009<0383:CBDPRO>2.0.CO;2.

Boodoo, S., D. Hudak, A. Ryzhkov, P. Zhang, N. Donaldson, D. Sills, and J. Reid, 2015: Quantitative precipitation estimation from a C-band dual-polarized radar for the 8 July 2013 flood in Toronto, Canada. *J. Hydrometeor.*, **16**, 2027–2044, https://doi.org/10.1175/JHM-D-15-0003.1.

Borowska, L., D. S. Zrnić, A. V. Ryzhkov, P. Zhang, and C. Simmer, 2011: Polarimetric estimates of a 1-month accumulation of light rain with a 3-cm wavelength radar. *J. Hydrometeor.*, **12**, 1024–1039, https://doi.org/10.1175/2011JHM1339.1.

Brandes, E. A., G. Zhang, and J. Vivekanandan, 2002: Experiments in rainfall estimation with a polarimetric radar in a subtropical environment. *J. Appl. Meteor.*, **41**, 674–685, https://doi.org/10.1175/1520-0450(2002)041<0674:EIREWA>2.0.CO;2; Corrigendum, **44**, 186, https://doi.org/10.1175/1520-0450(2005)44<186:C>2.0.CO;2.

——, ——, and ——, 2004: Comparison of polarimetric radar drop size distribution retrieval algorithms. *J. Atmos. Oceanic Technol.*, **21**, 584–598, https://doi.org/10.1175/1520-0426(2004)021<0584:COPRDS>2.0.CO;2.

Bringi, V. N., and V. Chandrasekar, 2001: *Polarimetric Doppler Weather Radar: Principles and Applications.* Cambridge University Press, 636 pp.

——, ——, N. Balakrishnan, and D. S. Zrnić, 1990: An examination of propagation effects in rainfall on radar measurements at microwave frequencies. *J. Atmos. Oceanic Technol.*, **7**,

829–840, https://doi.org/10.1175/1520-0426(1990)007<0829:AEOPEI>2.0.CO;2.

——, G.-J. Huang, V. Chandrasekar, and T. D. Keenan, 2001: An areal rainfall estimator using differential propagation phase: Evaluation using a C-band radar and a dense gauge network in the tropics. *J. Atmos. Oceanic Technol.*, **18**, 1810–1818, https://doi.org/10.1175/1520-0426(2001)018<1810:AAREUD>2.0.CO;2.

——, V. Chandrasekar, J. Hubbert, E. Gorgucci, W. L. Randeu, and M. Schoenhuber, 2003: Raindrop size distribution in different climatic regimes from disdrometer and dual-polarized radar analysis. *J. Atmos. Sci.*, **60**, 354–365, https://doi.org/10.1175/1520-0469(2003)060<0354:RSDIDC>2.0.CO;2.

——, M. Thurai, K. Nakagawa, G. J. Huang, T. Kobayashi, A. Adachi, H. Hanado, and S. Sekizawa, 2006: Rainfall estimation from C-band polarimetric radar in Okinawa, Japan: Comparisons with 2D-video disdrometer and 400 MHz wind profiler. *J. Meteor. Soc. Japan*, **84**, 705–724, https://doi.org/10.2151/jmsj.84.705.

——, C. R. Williams, M. Thurai, and P. T. May, 2009: Using dual-polarized radar and dual-frequency profiler for DSD characterization: A case study from Darwin, Australia. *J. Atmos. Oceanic Technol.*, **26**, 2107–2122, https://doi.org/10.1175/2009JTECHA1258.1.

——, M. A. Rico-Ramirez, and M. Thurai, 2011: Rainfall estimation with an operational polarimetric C-band radar in the United Kingdom: Comparison with a gauge network and error analysis. *J. Hydrometeor.*, **12**, 935–954, https://doi.org/10.1175/JHM-D-10-05013.1.

——, G.-J. Huang, S. J. Munchak, C. D. Kummerow, D. A. Marks, and D. B. Wolff, 2012: Comparison of drop size distribution parameter (D_0) and rain rate from S-band dual-polarized ground radar, TRMM Precipitation radar (PR), and combined PR–TMI: Two events from Kwajalein Atoll. *J. Atmos. Oceanic Technol.*, **29**, 1603–1616, https://doi.org/10.1175/JTECH-D-11-00153.1.

Carey, L. D., and S. A. Rutledge, 2000: The relationship between precipitation and lightning in tropical island convection: A C-band polarimetric radar study. *Mon. Wea. Rev.*, **128**, 2687–2710, https://doi.org/10.1175/1520-0493(2000)128<2687:TRBPAL>2.0.CO;2.

——, and W. A. Petersen, 2015: Sensitivity of C-band polarimetric radar–based drop size estimates to maximum diameter. *J. Appl. Meteor. Climatol.*, **54**, 1352–1371, https://doi.org/10.1175/JAMC-D-14-0079.1.

——, S. A. Rutledge, D. A. Ahijevych, and T. D. Keenan, 2000: Correcting propagation effects in C-band polarimetric radar observations of tropical convection using differential propagation phase. *J. Appl. Meteor.*, **39**, 1405–1433, https://doi.org/10.1175/1520-0450(2000)039<1405:CPEICB>2.0.CO;2.

Chandrasekar, V., V. N. Bringi, N. Balakrishnan, and D. S. Zrnić, 1990: Error structure of multiparameter radar and surface measurements of rainfall. Part III: Specific differential phase. *J. Atmos. Oceanic Technol.*, **7**, 621–629, https://doi.org/10.1175/1520-0426(1990)007<0621:ESOMRA>2.0.CO;2.

——, E. Gorgucci, and G. Scarchilli, 1993: Optimization of multiparameter radar estimates of rainfall. *J. Appl. Meteor.*, **32**, 1288–1293, https://doi.org/10.1175/1520-0450(1993)032<1288:OOMREO>2.0.CO;2.

Cifelli, R., C. R. Williams, D. K. Rajopadhyaya, S. K. Avery, K. S. Gage, and P. T. May, 2000: Drop-size distribution characteristics in tropical mesoscale convective systems. *J. Appl. Meteor.*, **39**, 760–777, https://doi.org/10.1175/1520-0450(2000)039<0760:DSDCIT>2.0.CO;2.

——, V. Chandrasekar, S. Lim, P. C. Kennedy, Y. Wang, and S. A. Rutledge, 2011: A new dual-polarization radar rainfall algorithm: Application in Colorado precipitation events. *J. Atmos. Oceanic Technol.*, **28**, 352–364, https://doi.org/10.1175/2010JTECHA1488.1.

Cotton, W. R., G. H. Bryan, and S. C. Van den Heever, 2011: *Storm and Cloud Dynamics.* International Geophysics Series, Vol. 99, Academic Press, 809 pp.

Diederich, M., A. Ryzhkov, C. Simmer, P. Zhang, and S. Trömel, 2015a: Use of specific attenuation for rainfall measurement at X-band radar wavelengths. Part I: Radar calibration and partial beam blockage estimation. *J. Hydrometeor.*, **16**, 487–502, https://doi.org/10.1175/JHM-D-14-0066.1.

——, ——, ——, ——, and ——, 2015b: Use of specific attenuation for rainfall measurement at X-band radar wavelengths. Part II: Rainfall estimates and comparison with rain gauges. *J. Hydrometeor.*, **16**, 503–516, https://doi.org/10.1175/JHM-D-14-0067.1.

Dolan, B., S. A. Rutledge, S. Lim, V. Chandrasekar, and M. Thurai, 2013: A robust C-band hydrometeor identification algorithm and application to a long-term polarimetric radar dataset. *J. Appl. Meteor. Climatol.*, **52**, 2162–2186, https://doi.org/10.1175/JAMC-D-12-0275.1.

Gatlin, P. N., M. Thurai, V. N. Bringi, W. Petersen, D. B. Wolff, A. Tokay, L. D. Carey, and M. Wingo, 2015: Searching for large raindrops: A global summary of two-dimensional video disdrometer observations. *J. Appl. Meteor. Climatol.*, **54**, 1069–1089, https://doi.org/10.1175/JAMC-D-14-0089.1.

Giangrande, S. E., M. J. Bartholomew, M. Pope, S. Collis, and M. P. Jensen, 2014: A summary of precipitation characteristics from the 2006–2011 northern Australian wet seasons as revealed by ARM disdrometer research facilities (Darwin, Australia). *J. Appl. Meteor. Climatol.*, **53**, 1213–1231, https://doi.org/10.1175/JAMC-D-13-0222.1.

Gorgucci, E., G. Scarchilli, and V. Chandrasekar, 1994: A robust estimator of rainfall rate using differential reflectivity. *J. Atmos. Oceanic Technol.*, **11**, 586–592, https://doi.org/10.1175/1520-0426(1994)011<0586:AREORR>2.0.CO;2.

Gu, J.-Y., A. Ryzhkov, P. Zhang, P. Neilley, M. Knight, B. Wolf, and D.-I. Lee, 2011: Polarimetric attenuation correction in heavy rain at C band. *J. Appl. Meteor. Climatol.*, **50**, 39–58, https://doi.org/10.1175/2010JAMC2258.1.

Hartmann, D. L., H. H. Hendon, and R. A. Houze Jr., 1984: Some implications of the mesoscale circulations in tropical cloud clusters for large-scale dynamics and climate. *J. Atmos. Sci.*, **41**, 113–121, https://doi.org/10.1175/1520-0469(1984)041<0113:SIOTMC>2.0.CO;2.

Hegerl, G. C., and Coauthors, 2015: Challenges in quantifying changes in the global water cycle. *Bull. Amer. Meteor. Soc.*, **96**, 1097–1115, https://doi.org/10.1175/BAMS-D-13-00212.1.

Houze, R. A., Jr., 1997: Stratiform precipitation in regions of convection: A meteorological paradox? *Bull. Amer. Meteor. Soc.*, **78**, 2179–2196, https://doi.org/10.1175/1520-0477(1997)078<2179:SPIROC>2.0.CO;2.

——, K. L. Rasmussen, M. D. Zuluaga, and S. R. Brodzik, 2015: The variable nature of convection in the tropics and subtropics: A legacy of 16 years of the Tropical Rainfall Measuring Mission satellite. *Rev. Geophys.*, **53**, 994–1021, https://doi.org/10.1002/2015RG000488.

Huang, G.-J., V. N. Bringi, and M. Thurai, 2008: Orientation angle distributions of drops after an 80-m fall using a 2D video disdrometer. *J. Atmos. Oceanic Technol.*, **25**, 1717–1723, https://doi.org/10.1175/2008JTECHA1075.1.

Hudlow, M. D., 1979: Mean rainfall patterns for the three phases of GATE. *J. Appl. Meteor.*, **18**, 1656–1669, https://doi.org/10.1175/1520-0450(1979)018<1656:MRPFTT>2.0.CO;2.

Illingworth, A. J., and T. M. Blackman, 2002: The need to represent raindrop size spectra as normalized gamma distributions for the interpretation of polarization radar observations. *J. Appl. Meteor.*, **41**, 286–297, https://doi.org/10.1175/1520-0450(2002)041<0286:TNTRRS>2.0.CO;2.

Jameson, A. R., 1992: The effect of temperature on attenuation-correction schemes in rain using polarization propagation differential phase shift. *J. Appl. Meteor.*, **31**, 1106–1118, https://doi.org/10.1175/1520-0450(1992)031<1106:TEOTOA>2.0.CO;2.

Johnson, R. H., T. M. Rickenbach, S. A. Rutledge, P. E. Ciesielski, and W. H. Schubert, 1999: Trimodal characteristics of tropical convection. *J. Climate*, **12**, 2397–2418, https://doi.org/10.1175/1520-0442(1999)012<2397:TCOTC>2.0.CO;2.

Keenan, T. D., L. D. Carey, D. S. Zrnić, and P. T. May, 2001: Sensitivity of 5-cm wavelength polarimetric radar variables to raindrop axial ratio and drop size distribution. *J. Appl. Meteor.*, **40**, 526–545, https://doi.org/10.1175/1520-0450(2001)040<0526:SOCWPR>2.0.CO;2.

Kumjian, M. R., 2013a: Principles and applications of dual-polarization weather radar. Part I: Description of the polarimetric radar variables. *J. Oper. Meteor.*, **1**, 226–242, https://doi.org/10.15191/nwajom.2013.0119.

——, 2013b: Principles and applications of dual-polarization weather radar. Part II: Warm- and cold-season applications. *J. Oper. Meteor.*, **1**, 243–264, https://doi.org/10.15191/nwajom.2013.0120.

——, 2013c: Principles and applications of dual-polarization weather radar. Part III: Artifacts. *J. Oper. Meteor.*, **1**, 265–274, https://doi.org/10.15191/nwajom.2013.0121.

——, and A. V. Ryzhkov, 2010: The impact of evaporation on polarimetric characteristics of rain: Theoretical model and practical implications. *J. Appl. Meteor. Climatol.*, **49**, 1247–1267, https://doi.org/10.1175/2010JAMC2243.1.

——, and ——, 2012: The impact of size sorting on the polarimetric radar variables. *J. Atmos. Sci.*, **69**, 2042–2060, https://doi.org/10.1175/JAS-D-11-0125.1.

Larsen, M. L., and K. A. O'Dell, 2016: Sampling variability effects in drop-resolving disdrometer observations. *J. Geophys. Res. Atmos.*, **121**, 11 777–11 791, https://doi.org/10.1002/2016JD025491.

Liu, N., and C. Liu, 2016: Global distribution of deep convection reaching tropopause in 1 year GPM observations. *J. Geophys. Res. Atmos.*, **121**, 3824–3842, https://doi.org/10.1002/2015JD024430.

Marshall, J. S., and W. M. Palmer, 1948: The distribution of raindrops with size. *J. Meteor.*, **5**, 165–166, https://doi.org/10.1175/1520-0469(1948)005<0165:TDORWS>2.0.CO;2.

Matrosov, S. Y., R. Cifelli, P. C. Kennedy, S. W. Nesbitt, S. A. Rutledge, V. N. Bringi, and B. E. Martner, 2006: A comparative study of rainfall retrievals based on specific differential phase shifts at X- and S-band radar frequencies. *J. Atmos. Oceanic Technol.*, **23**, 952–963, https://doi.org/10.1175/JTECH1887.1.

May, P. T., and T. D. Keenan, 2005: Evaluation of microphysical retrievals from polarimetric radar with wind profiler data. *J. Appl. Meteor.*, **44**, 827–838, https://doi.org/10.1175/JAM2230.1.

——, A. R. Jameson, T. D. Keenan, P. E. Johnston, and C. Lucas, 2002: Combined wind profiler/polarimetric radar studies of the vertical motion and microphysical characteristics of tropical seabreeze thunderstorms. *Mon. Wea. Rev.*, **130**, 2228–2239, https://doi.org/10.1175/1520-0493(2002)130<2228:CWPPRS>2.0.CO;2.

Munchak, S. J., C. D. Kummerow, and G. Elsaesser, 2012: Relationships between the raindrop size distribution and properties of the environment and clouds inferred from TRMM. *J. Climate*, **25**, 2963–2978, https://doi.org/10.1175/JCLI-D-11-00274.1.

Nguyen, C. M., D. N. Moisseev, and V. Chandrasekar, 2008: A parametric time domain method for spectral moment estimation and clutter mitigation for weather radars. *J. Atmos. Oceanic Technol.*, **25**, 83–92, https://doi.org/10.1175/2007JTECHA927.1.

Park, S.-G., M. Maki, K. Iwanami, V. N. Bringi, and V. Chandrasekar, 2005: Correction of radar reflectivity and differential reflectivity for rain attenuation at X band. Part II: Evaluation and application. *J. Atmos. Oceanic Technol.*, **22**, 1633–1655, https://doi.org/10.1175/JTECH1804.1.

Pepler, A. S., and P. T. May, 2012: A robust error-based rain estimation method for polarimetric radar. Part II: Case study. *J. Appl. Meteor. Climatol.*, **51**, 1702–1713, https://doi.org/10.1175/JAMC-D-11-0159.1.

——, ——, and M. Thurai, 2011: A robust error-based rain estimation method for polarimetric radar. Part I: Development of a method. *J. Appl. Meteor. Climatol.*, **50**, 2092–2103, https://doi.org/10.1175/JAMC-D-10-05029.1.

Powell, S. W., R. A. Houze Jr., and S. R. Brodzik, 2016: Rainfall-type categorization of radar echoes using polar coordinate reflectivity data. *J. Atmos. Oceanic Technol.*, **33**, 523–538, https://doi.org/10.1175/JTECH-D-15-0135.1.

Pruppacher, H. R., and J. D. Klett, 1997: *Microphysics of Clouds and Precipitation.* 2nd ed. Kluwer Academic, 954 pp.

Rowe, A. K., and R. A. Houze Jr., 2014: Microphysical characteristics of MJO convection over the Indian Ocean during DYNAMO. *J. Geophys. Res. Atmos.*, **119**, 2543–2554, https://doi.org/10.1002/2013JD020799.

Ryzhkov, A. V., and D. S. Zrnić, 1995: Comparison of dual-polarization radar estimators of rain. *J. Atmos. Oceanic Technol.*, **12**, 249–256, https://doi.org/10.1175/1520-0426(1995)012<0249:CODPRE>2.0.CO;2.

——, ——, and D. Atlas, 1997: Polarimetrically tuned $R(Z)$ relations and comparison of radar rainfall methods. *J. Appl. Meteor.*, **36**, 340–349, https://doi.org/10.1175/1520-0450(1997)036<0340:PTRZRA>2.0.CO;2.

——, S. E. Giangrande, V. M. Melnikov, and T. J. Schuur, 2005a: Calibration issues of dual-polarization radar measurements. *J. Atmos. Oceanic Technol.*, **22**, 1138–1155, https://doi.org/10.1175/JTECH1772.1.

——, ——, and T. J. Schuur, 2005b: Rainfall estimation with a polarimetric prototype of WSR-88D. *J. Appl. Meteor.*, **44**, 502–525, https://doi.org/10.1175/JAM2213.1.

——, T. J. Schuur, D. W. Burgess, P. L. Heinselman, S. E. Giangrande, and D. S. Zrnić, 2005c: The Joint Polarization Experiment: Polarimetric rainfall measurements and hydrometeor classification. *Bull. Amer. Meteor. Soc.*, **86**, 809–824, https://doi.org/10.1175/BAMS-86-6-809.

——, M. Diederich, P. Zhang, and C. Simmer, 2014: Potential utilization of specific attenuation for rainfall estimation, mitigation of partial beam blockage, and radar networking. *J. Atmos. Oceanic Technol.*, **31**, 599–619, https://doi.org/10.1175/JTECH-D-13-00038.1.

Sachidananda, M., and D. S. Zrnić, 1986: Differential propagation phase shift and rainfall rate estimation. *Radio Sci.*, **21**, 235–247, https://doi.org/10.1029/RS021i002p00235.

——, and ——, 1987: Rain rate estimates from differential polarization measurements. *J. Atmos. Oceanic Technol.*, **4**, 588–598, https://doi.org/10.1175/1520-0426(1987)004<0588:RREFDP>2.0.CO;2.

Scarchilli, G., E. Gorgucci, V. Chandrasekar, and T. A. Seliga, 1993: Rainfall estimation using polarimetric techniques at C-band frequencies. *J. Appl. Meteor.*, **32**, 1150–1160, https://doi.org/10.1175/1520-0450(1993)032<1150:REUPTA>2.0.CO;2.

Schönhuber, M., G. Lammer, and W. L. Randeu, 2007: One decade of imaging precipitation measurement by 2D-video-disdrometer. *Adv. Geosci.*, **10**, 85–90, https://doi.org/10.5194/adgeo-10-85-2007.

——, ——, and ——, 2008: The 2D-video-disdrometer. *Precipitation: Advances in Measurement, Estimation and Prediction*, S. C. Michaelides, Ed., Springer, 3–31 pp.

Schumacher, C., and R. A. Houze Jr., 2003: The TRMM Precipitation Radar's view of shallow, isolated rain. *J. Appl. Meteor.*, **42**, 1519–1524, https://doi.org/10.1175/1520-0450(2003)042<1519:TTPRVO>2.0.CO;2.

——, ——, and I. Kraucunas, 2004: The tropical dynamical response to latent heating estimates derived from the TRMM Precipitation Radar. *J. Atmos. Sci.*, **61**, 1341–1358, https://doi.org/10.1175/1520-0469(2004)061<1341:TTDRTL>2.0.CO;2.

——, S. N. Stevenson, and C. R. Williams, 2015: Vertical motions of the tropical convective cloud spectrum over Darwin, Australia. *Quart. J. Roy. Meteor. Soc.*, **141**, 2277–2288, https://doi.org/10.1002/qj.2520.

Schuur, T. J., A. V. Ryzhkov, D. S. Zrnić, and M. Schönhuber, 2001: Drop size distributions measured by a 2D video disdrometer: Comparison with dual-polarization radar data. *J. Appl. Meteor.*, **40**, 1019–1034, https://doi.org/10.1175/1520-0450(2001)040<1019:DSDMBA>2.0.CO;2.

Seliga, T. A., and V. N. Bringi, 1976: Potential use of radar differential reflectivity measurements at orthogonal polarizations for measuring precipitation. *J. Appl. Meteor.*, **15**, 69–76, https://doi.org/10.1175/1520-0450(1976)015<0069:PUORDR>2.0.CO;2.

Short, D. A., P. A. Kucera, B. S. Ferrier, J. C. Gerlach, S. A. Rutledge, and O. W. Thiele, 1997: Shipboard radar rainfall patterns within the TOGA COARE IFA. *Bull. Amer. Meteor. Soc.*, **78**, 2817–2836, https://doi.org/10.1175/1520-0477(1997)078<2817:SRRPWT>2.0.CO;2.

Skofronick-Jackson, G., and Coauthors, 2017: The Global Precipitation Measurement (GPM) mission for science and society. *Bull. Amer. Meteor. Soc.*, **98**, 1679–1695, https://doi.org/10.1175/BAMS-D-15-00306.1.

Smith, P. L., 2016: Sampling issues in estimating radar variables from disdrometer data. *J. Atmos. Oceanic Technol.*, **33**, 2305–2313, https://doi.org/10.1175/JTECH-D-16-0040.1.

Steiner, M., R. A. Houze Jr., and S. E. Yuter, 1995: Climatological characterization of three-dimensional storm structure from operational radar and rain gauge data. *J. Appl. Meteor.*, **34**, 1978–2007, https://doi.org/10.1175/1520-0450(1995)034<1978:CCOTDS>2.0.CO;2.

——, J. A. Smith, and R. Uijlenhoet, 2004: A microphysical interpretation of radar reflectivity–rain rate relationships. *J. Atmos. Sci.*, **61**, 1114–1131, https://doi.org/10.1175/1520-0469(2004)061<1114:AMIORR>2.0.CO;2.

Tan, J., W. A. Petersen, P.-E. Kirstetter, and Y. Tian, 2017: Performance of IMERG as a function of spatiotemporal scale. *J. Hydrometeor.*, **18**, 307–319, https://doi.org/10.1175/JHM-D-16-0174.1.

Testud, J., E. Le Bouar, E. Obligis, and M. Ali-Mehenni, 2000: The rain profiling algorithm applied to polarimetric weather radar. *J. Atmos. Oceanic Technol.*, **17**, 332–356, https://doi.org/10.1175/1520-0426(2000)017<0332:TRPAAT>2.0.CO;2.

Thompson, E. J., S. A. Rutledge, B. Dolan, and M. Thurai, 2015: Drop size distributions and radar observations of convective and stratiform rain over the equatorial Indian and west Pacific Oceans. *J. Atmos. Sci.*, **72**, 4091–4125, https://doi.org/10.1175/JAS-D-14-0206.1.

Thurai, M., G. J. Huang, V. N. Bringi, W. L. Randeu, and M. Schönhuber, 2007: Drop shapes, model comparisons, and calculations of radar parameters in rain. *J. Atmos. Oceanic Technol.*, **24**, 1019–1032, https://doi.org/10.1175/JTECH2051.1.

——, V. N. Bringi, and P. T. May, 2010: CPOL radar-derived drop size distribution statistics of stratiform and convective rain for two regimes in Darwin, Australia. *J. Atmos. Oceanic Technol.*, **27**, 932–942, https://doi.org/10.1175/2010JTECHA1349.1.

——, K. V. Mishra, V. N. Bringi, and W. F. Krajewski, 2017: Initial results of a new composite-weighted algorithm for dual-polarized X-band rainfall estimation. *J. Hydrometeor.*, **18**, 1081–1100, https://doi.org/10.1175/JHM-D-16-0196.1.

Tokay, A., and D. A. Short, 1996: Evidence from tropical raindrop spectra of the origin of rain from stratiform versus convective clouds. *J. Appl. Meteor.*, **35**, 355–371, https://doi.org/10.1175/1520-0450(1996)035<0355:EFTRSO>2.0.CO;2.

——, A. Kruger, and W. F. Krajewski, 2001: Comparison of drop size distribution measurements by impact and optical disdrometers. *J. Appl. Meteor.*, **40**, 2083–2097, https://doi.org/10.1175/1520-0450(2001)040<2083:CODSDM>2.0.CO;2.

——, P. G. Bashor, and K. R. Wolff, 2005: Error characteristics of rainfall measurements by collocated Joss–Waldvogel disdrometers. *J. Atmos. Oceanic Technol.*, **22**, 513–527, https://doi.org/10.1175/JTECH1734.1.

——, W. A. Petersen, P. Gatlin, and M. Wingo, 2013: Comparison of raindrop size distribution measurements by collocated disdrometers. *J. Atmos. Oceanic Technol.*, **30**, 1672–1690, https://doi.org/10.1175/JTECH-D-12-00163.1.

Wang, Y., J. Zhang, A. V. Ryzhkov, and L. Tang, 2013: C-band polarimetric radar QPE based on specific differential propagation phase for extreme typhoon rainfall. *J. Atmos. Oceanic Technol.*, **30**, 1354–1370, https://doi.org/10.1175/JTECH-D-12-00083.1.

——, P. Zhang, A. V. Ryzhkov, J. Zhang, and P.-L. Chang, 2014: Utilization of specific attenuation for tropical rainfall estimation in complex terrain. *J. Hydrometeor.*, **15**, 2250–2266, https://doi.org/10.1175/JHM-D-14-0003.1.

Xu, W., and S. A. Rutledge, 2014: Convective characteristics of the Madden–Julian oscillation over the central Indian Ocean observed by shipborne radar during DYNAMO. *J. Atmos. Sci.*, **71**, 2859–2877, https://doi.org/10.1175/JAS-D-13-0372.1.

Yoneyama, K., and Coauthors, 2008: MISMO field experiment in the equatorial Indian Ocean. *Bull. Amer. Meteor. Soc.*, **89**, 1889–1903, https://doi.org/10.1175/2008BAMS2519.1.

Yuter, S. E., and R. A. Houze Jr., 1998: The natural variability of precipitating clouds over the western Pacific warm pool. *Quart. J. Roy. Meteor. Soc.*, **124**, 53–99, https://doi.org/10.1002/qj.49712454504.

Zipser, E. J., 2003: Some views on "hot towers" after 50 years of tropical field programs and two years of TRMM data. *Cloud Systems, Hurricanes, and the Tropical Rainfall Measuring Mission (TRMM)*, *Meteor. Monogr.*, No. 51, Amer. Meteor. Soc., 49–58.

Zrnić, D. S., T. D. Keenan, L. D. Carey, and P. May, 2000: Sensitivity analysis of polarimetric variables at a 5-cm wavelength in rain. *J. Appl. Meteor.*, **39**, 1514–1526, https://doi.org/10.1175/1520-0450(2000)039<1514:SAOPVA>2.0.CO;2.